Geodynamics Series Volume 25

Contributions of Space Geodesy to Geodynamics:
Technology

Millimeter Accuracy Satellite Laser Ranging: A Review

John J. Degnan

Page01.jpg

Millimeter Accuracy Satellite Laser Ranging: A Review

JOHN J. DEGNAN

Code 920.1/Space Geodesy and Altimetry Projects Office, NASA/Goddard Space Flight Center, Greenbelt, MD 20771 USA

The present paper reviews: (1) recent developments in the field of satellite laser ranging including the status of the global network, growth of the scientific user community and satellite constellation, and improvements in system precision; (2) the radar link equation and related mathematical models used in the computation of signal strength, false alarm rates, and detection probabilities for SLR systems; (3) spherical shell models of the atmosphere currently used by analysts to correct for refraction in single color systems; and (4) two color techniques for directly measuring atmospheric delay. The various models are combined with an overview of laser and detector technology to develop a wavelength figure of merit for fourth generation two color systems which utilize harmonic generation in crystals or Raman shifting in gases to generate the dual wavelengths. The paper also provides an overview of retroreflector theory, which includes a brief discussion of velocity aberration and retroreflector spoiling techniques, and develops a simple analytical model of a spherical geodetic satellite which permits the approximate computation of satellite target cross-section and impulse response. The model is then applied to the design of future geodetic satellites capable of supporting millimeter accuracy two color measurements. The final section of the paper provides a summary statement and offers some concluding remarks.

1. INTRODUCTION

In the seven years since the last review of satellite laser ranging (SLR) technology was published [Degnan, 1985], several important developments have occurred. These include: (1) substantial growth in the size of the international network of SLR stations, both fixed and mobile; (2) overall improvement in the ranging precision of the global SLR network; (3) a rapidly growing constellation of space geodetic and other target satellites; (4) an expanded scientific user community; (5) improved coordination with proponents of other space geodetic techniques, such as Very Long Baseline Interferometry (VLBI) and the Global Positioning System (GPS), and (6) the emergence of the CERGA station in Grasse (France) as the world's most prolific lunar laser ranging (LLR) station. Section 2 of this paper provides an overview of recent developments in the international laser network.

Modern SLR systems produce subcentimeter single shot precisions and precisions of 1 to 3 mm for normal point (time-averaged) data. Thus, the timing accuracy of SLR field hardware is no longer believed to be the principle limitation on the absolute accuracy of the range measurement. Instead, the limiting error source (at roughly the one cm level) is the propagation delay uncertainty associated with the atmospheric transmission channel. Thus, the principal thrust of fourth-generation SLR system development is to achieve millimeter absolute accuracy ranging through the direct measurement of the atmospheric propagation delay via two color techniques [Degnan, 1985; Abshire and Gardner, 1985].

Over the past three years, the author has had the opportunity to visit many of the foreign SLR stations which have provided, or will soon provide data, to the Crustal Dynamics Project and its successor NASA Dynamics of the Solid Earth (DOSE) program. Many of the engineers at these stations have expressed an interest in the mathematical models which have been developed to assist in system design. Thus, while the 1985 review provided a non-mathematical tutorial on the subject of satellite ranging with an emphasis on understanding the characteristics and capabilities of the field hardware and operational techniques, the present review dwells more on the mathematical modeling of SLR systems in general and how these models influence the design of fourth generation two color systems. Section 3 introduces the radar link equation used by engineers to compute important SLR system parameters (e.g. signal strength, probability of detection, false alarm rates, etc.) and discusses in detail the various terms which appear in that equation. Some sample calculations are carried out for a NASA MOBLAS station.

Section 4 provides an overview of atmospheric models used to obtain a range correction in single color systems and introduces the concept of two color ranging for absolute range correction. Section 5 attempts to combine the theoretical results of Sections

Contributions of Space Geodesy to Geodynamics: Technology
Geodynamics 25
This paper is not subject to U.S. copyright. Published in 1993 by the American Geophysical Union.

Page02.jpg

3 and 4 with a discussion of practical hardware limitations to define "optimum" wavelengths for two color SLR systems.

The two color technique requires picosecond precision measurement of the differential time of flight. Unfortunately, the substantial pulse-spreading effects of many existing target satellites, which were originally designed to support centimeter accuracy measurements, make the achievement of this ultraprecise timing precision more difficult. Therefore, Section 6 reviews some basic theory of spaceborne retroreflector arrays, considers the optical signal returns and pulse spreading effects from existing target satellites in terms of their utility for early two color field tests, and considers the feasibility of future millimeter accuracy satellites capable of supporting two color investigations. Section 7 offers some concluding remarks.

The basic hardware approaches to two color measurements and early laboratory and horizontal range experiments were reviewed previously [Degnan, 1985; Abshire and Gardner, 1985] and will not be repeated here. However, a companion article in this volume [Zagwodzki et al., 1993] describes in detail a prototype two color SLR system undergoing field tests at the Goddard Space Flight Center in Greenbelt, Maryland, and presents some streak camera waveforms obtained from retroreflectors on the Relay Mirror Experiment (RME) satellite during Fall, 1991. A second companion article [Varghese et al., 1993] describes recent progress in the development of calibration techniques and readout systems for streak tube receivers. Since streak tube receivers are characterized by large data volumes (~64 K per streak camera frame), special readout devices had to be developed to reduce data transfer and storage requirements [Varghese et al., 1992]. Both of these research activities have been supported by NASA's Crustal Dynamics Project.

While the present review does not specifically address the technology and scientific accomplishments of lunar laser ranging in recent years, clearly the technical information presented here is highly relevant to the ranging of our most distant satellite. The technological status of lunar laser ranging is covered in companion articles [Veillet et al., 1993; Shelus et al., 1993] located elsewhere in this volume.

2. Recent Developments (1985-1992)

2.1 International SLR Network and Reference Frames

Approximately 43 SLR systems now contribute data regularly to NASA's Crustal Dynamics Project, and several other stations are near completion. Figure 1 illustrates the present status of the international SLR network including both fixed and mobile sites. Together with the VLBI technique, SLR has provided a truly global view of tectonic plate motion accurate to a few millimeters per year [Smith et al., 1990]. Global intercomparisons of collocated SLR/VLBI sites show agreement between the two techniques at about the two cm level (one sigma RMS) in all three station position coordinates [Ray et al., 1991] and an agreement in scale at about one part per billion [Himwich et al., 1993]. Together, the SLR and VLBI techniques presently define the International Terrestrial Reference Frame (ITRF) with SLR uniquely defining the reference origin, i.e. the location of the Earth center of mass. SLR and VLBI also provide highly accurate information on Earth orientation (polar nutation and wobble) and spin rate (length of day), and both data sets are routinely forwarded to the International Earth Rotation Service (IERS) in Paris, France. During an intensive campaign in 1991, GPS also demonstrated an impressive capability to provide high time resolution Earth orientation data [Robertson, 1991].

2.2 SLR Support for Altimetric Missions

As we enter the 1990's, the global SLR network is being tasked to provide the link between the ITRF and various spaceborne altimetric missions designed to study sea and ice surface topography. By combining microwave altimetry data with the precise orbital ephemerides derived from SLR, one can calibrate the onboard altimeter and express the topographic data within the context of the ITRF thereby enhancing our ability to monitor global ocean circulation, mean sea level, and ice sheet thickness [Degnan, 1991].

Intensive support of oceanographic missions by the SLR network began in July 1991 following the launch of ERS-1. As a result of the unfortunate failure of the onboard Precise Range and Range-Rate Experiment (PRARE) instrument shortly after ERS-1 launch, SLR became the only source of precise orbital data. Many of the SLR stations transitioned to double shift operations in 1992 in preparation for a TOPEX/Poseidon launch in July 1992. This resulted in a significant increase in SLR data for all satellites. Similar SLR support for followon ERS, TOPEX, and GEOSAT ocean/ice missions are under discussion.

2.3 A Growing Constellation of Laser-Tracked Satellites

The constellation of actively tracked satellites grew from only two in 1985 (LAGEOS and STARLETTE) to six by the end of 1991 following the launches of AJISAI by Japan in 1987, ETALON I and II by the Soviet Union in 1989, and the European community's ERS-1 in 1991. In 1992, two additional satellites were tracked - TOPEX/Poseidon (US/France) and LAGEOS 2 (Italy). These are expected to be followed in subsequent years by two additional space geodetic satellites, STELLA (France-1993) and LAGEOS 3 (Italy-1995). The improving precision of SLR globally, combined with the growing constellation of space geodetic satellites at a variety of orbital altitudes and inclinations, will permit the further improvement of Earth gravity field models which are already complete through degree and order 50 [Lerch et al., 1992]. Multiple satellites will also drastically reduce the time required for an accurate geodetic fix using the SLR technique which, for most of its history, has relied on a single satellite, LAGEOS. However, even with just the LAGEOS and STARLETTE satellites, observed secular variations in the gravitational field components have already been interpreted in terms of mass redistributions associated with postglacial rebounding and ocean tides.

2.4 Transportable Systems and Regional Campaigns

In addition to the global network of fixed SLR stations, there are seven highly transportable systems operated by the United States

Page03.jpg

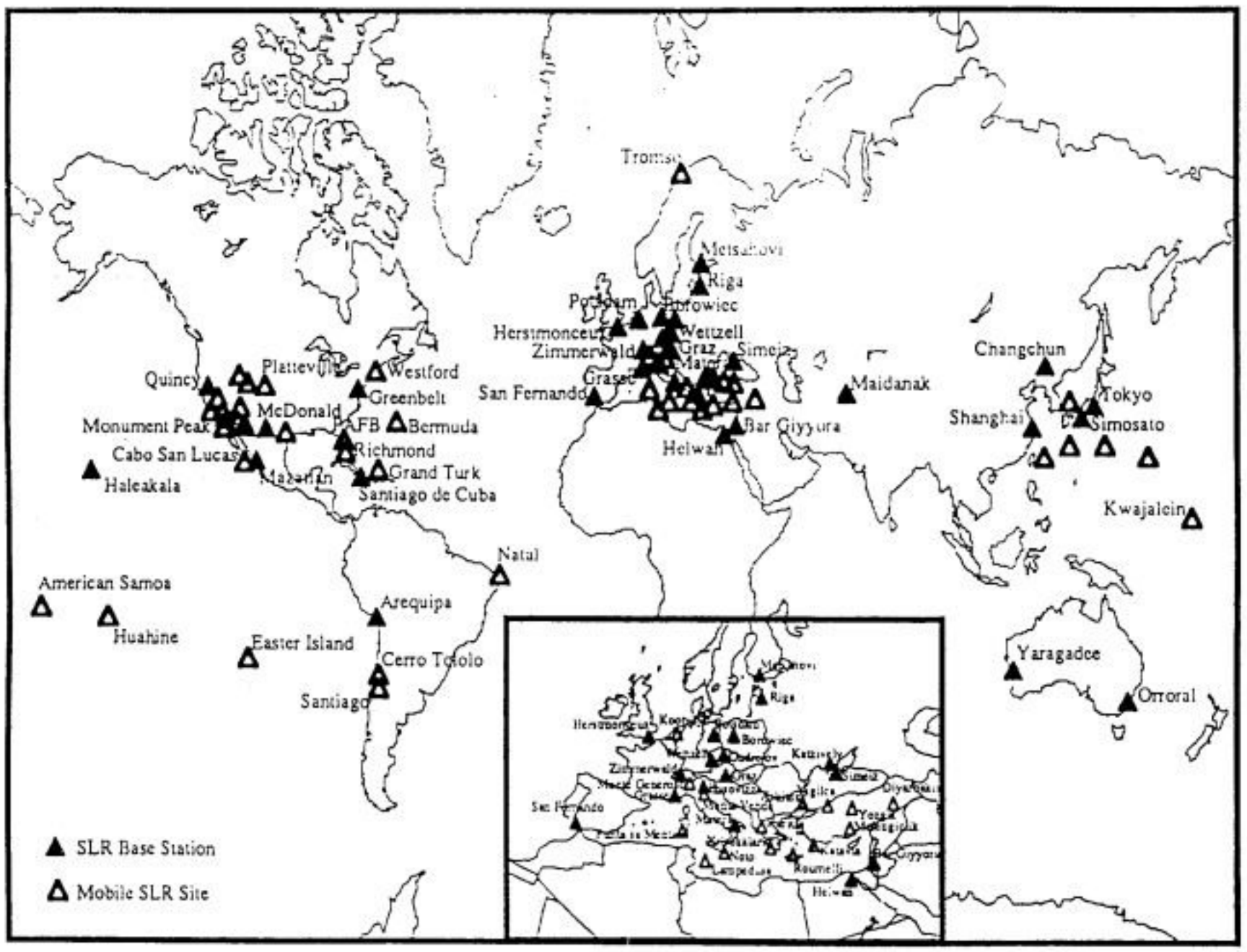

Fig. 1. International satellite laser ranging sites - fixed and mobile.

(4), Germany (1), Netherlands (1), and Japan (1). Additional mobile systems are under development in Germany, France, and Italy. Over the past decade, NASA and the European SLR community have successfully used highly transportable systems in intensive regional campaigns to study crustal deformation in the Mediterranean region and in the Southwest United States and Mexico. In order to provide a better understanding of the complex interactions between the Eurasian and African plates, future Mediterranean campaigns will adopt an integrated approach using all three space geodetic techniques in the expansion of regional measurements to the Azores in the West, to the Caspian Sea in the East, to the northernmost reaches of Europe, and deep into the African plate to the South.

It is the opinion of the author that, as GPS demonstrates its capability to take over the measurement of short and intermediate baselines in regional campaigns (through careful intercomparisons with the mobile SLR and VLBI results), the highly transportable SLR systems might be better utilized in the establishment of new fiducial or altimeter tracking sites in geographical regions where present controls are sparse, such as in Africa, Central Asia and the South Pacific and Indian Oceans.

2.5 Third Generation SLR System Precision

In an earlier review [Degnan, 1985], it was predicted that subcentimeter single-shot ranging precisions would become commonplace in the global network within a very few years. Since about 1987, most of the NASA Crustal Dynamics Satellite Laser Ranging (CDSLR) network has operated with single shot precisions between 7 to 10 mm (one sigma RMS) to geodetic satellites such as STARLETTE and LAGEOS [Degnan, 1989]. When one computes so-called "normal points" (i.e. temporal averages of single shot data designed to statistically reduce random errors in the measurement), the one sigma RMS scatter about the short arc orbit or high order polynomial fit at NASA sites is typically on the order of 1 to 3 mm.

In the past, the highly precise normal points were processed at a central facility from full rate data and typically were not available until about two months after the data was taken.

Page04.jpg

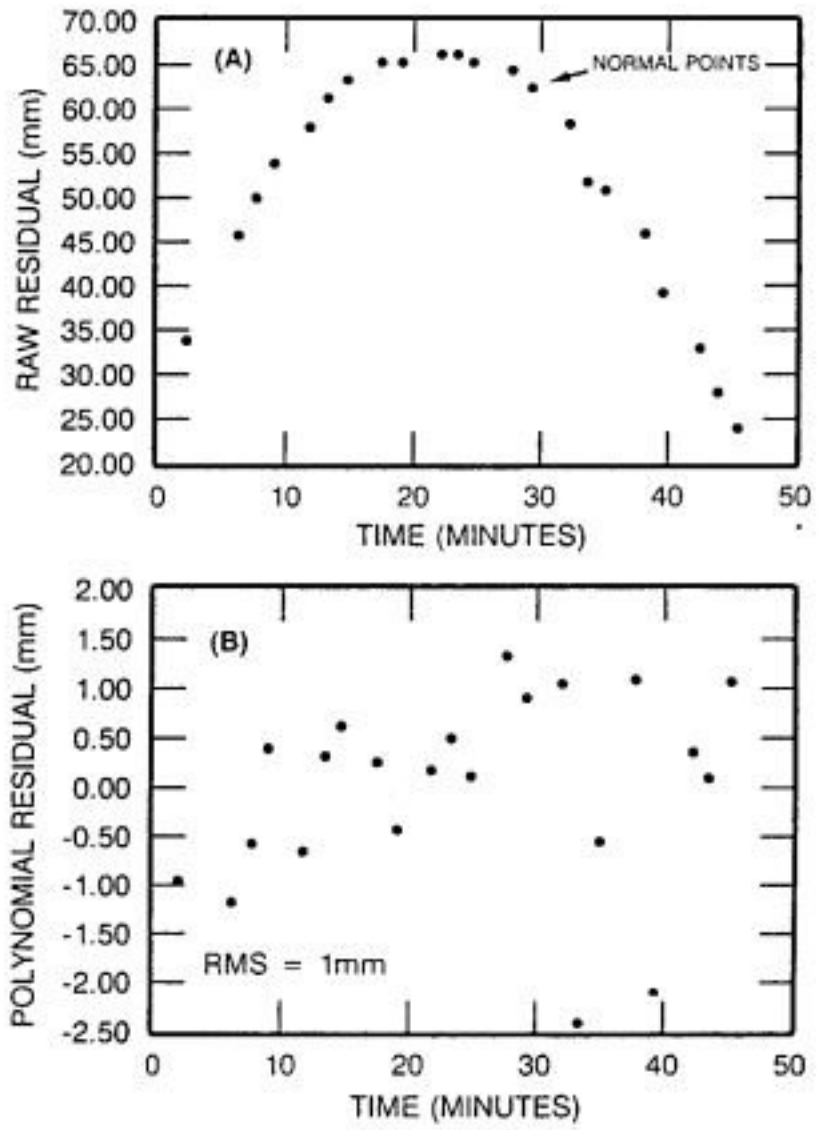

Fig. 2. (a) Fit of normal points, generated onsite at the MOBLAS 5 station in Yarragadee, Western Australia, to a nominal global orbit provided by the University of Texas Center for Space Research. (b) Residuals of same normal points following fit (1 mm RMS) of the raw residuals to a polynomial.

However, as a result of recent computer upgrades at the stations, normal points are now being computed onsite at many stations and transmitted within 24 hours to central archives such as the Crustal Dynamics Data Information System (CDDIS) at the Goddard Space Flight Center and the European Data Center (EDC) in Munich, Germany. Figure 2 shows a particularly good LAGEOS pass (high elevation, maximum number of normal points, 1 mm RMS) taken by the NASA MOBLAS-5 station at Yarragadee in Western Australia. In spite of these advances, however, the precision of individual sites within the international network is fairly nonuniform - ranging from subcentimeter to about 20 cm for single shot ranges and from about 1 mm to 4 cm for normal points.

In another important development, hardware-related systematics are now being determined and controlled at the few millimeter level through so-called "collocation" tests [Varghese et al., 1988]. In a collocation test, two or more systems, which are usually placed within about 60 meters of each other, simultaneously track a series of satellite passes. The close proximity between systems permits millimeter accuracy surveys of the displacement vectors between the system reference points and also results in a common atmospheric path between the stations and the satellite. In a collocation, one system is selected as the "standard," and its surveyed location and range data are used to compute a series of "ground truth" orbits. The survey data then permits a direct comparison of the measured ranges from the collocated systems with what is expected based on the range data from the reference standard. Figure 3 shows the excellent agreement between three NASA systems (MOBLAS-7, TLRS-1, and TLRS-4) during a rare three way collocation at the Goddard Space Flight Center in Greenbelt, Maryland.

The third generation SLR components and systems which produced these high precisions have been adequately described in an earlier review [Degnan, 1985] and in the proceedings of two international workshops on SLR instrumentation [Varghese and Heineck, 1986; Degnan, 1989] and hence will not be repeated here. However, it should be mentioned, for the sake of completeness, that comparable precisions have recently been

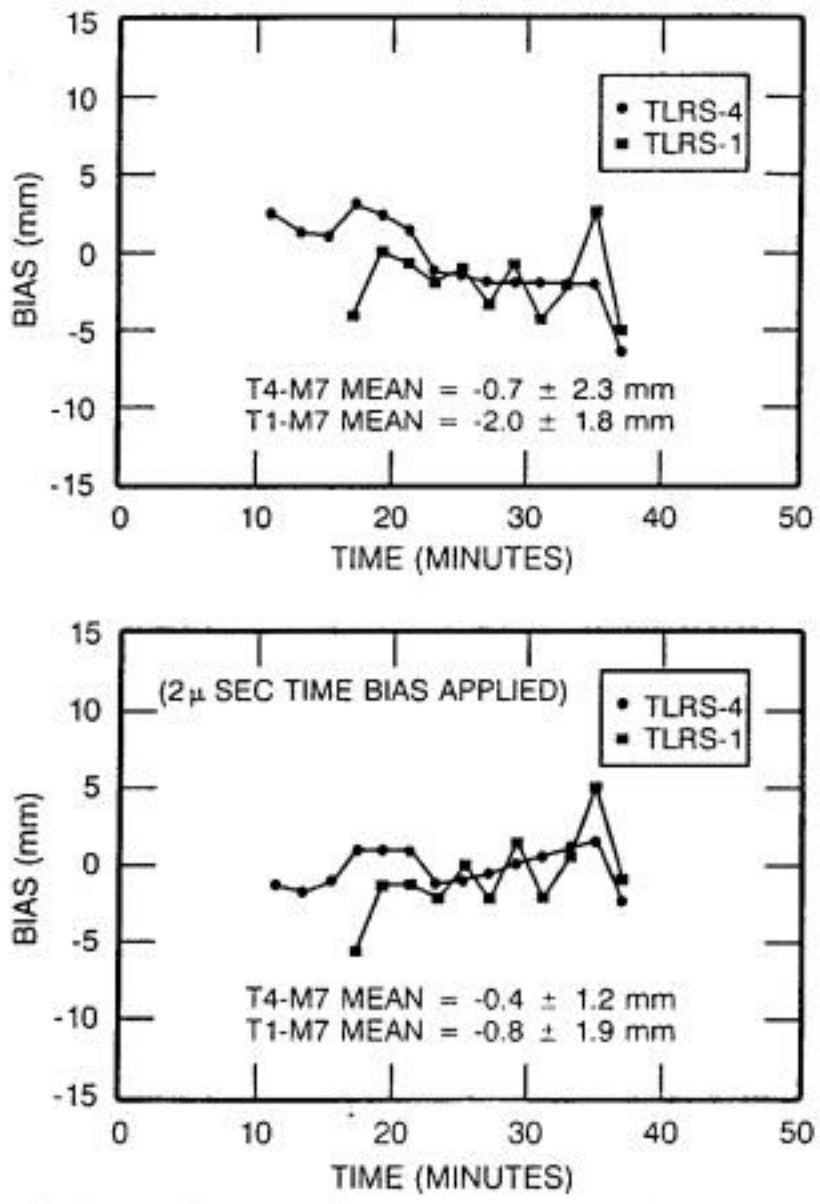

Fig. 3. Typical results from a three-way collocation between the MOBLAS 7 station and two NASA transportable systems showing agreement at the few millimeter level. Part (b) shows the improved agreement after a 2 microsecond time bias at the MOBLAS 7 station was removed.

Page05.jpg

obtained by European researchers using somewhat different hardware [e.g., Prochazka et al., 1990]. Specifically, these systems used a combination of shorter 35 picosecond laser pulsewidths (vs 150 picoseconds at the NASA sites) and avalanche photodiode detectors operated in the geiger mode (instead of microchannel plate photomultipliers followed by constant fraction discriminators).

3. Mathematical Model of SLR System Performance

3.1 The Radar Link Equation

The radar link equation is used by engineers to calculate the mean signal flux in their receivers. The mean number of photoelectrons n_{pe} recorded by the ranging detector is given by:

$$n_{pe}=\eta_q\left(E_T\frac{\lambda}{hc}\right)\eta_t G_t\sigma\left(\frac{1}{4\pi R^2}\right)^2 A_r\eta_r T_a^2 T_c^2 \qquad (3.1.1)$$

where η_q is the detector quantum efficiency, E_T is the laser pulse energy, λ is the laser wavelength, h is Planck's constant, c is the velocity of light in vacuum, η_t is the transmit optics efficiency, G_t is the transmitter gain, σ is the satellite optical cross-section (discussed in Section 6), R is the slant range to the target, A_r is the effective area of the telescope receive aperture, η_r is the efficiency of the receive optics, T_a is the one-way atmospheric transmission, and T_c is the one way transmissivity of cirrus clouds (when present). The slant range R is given by the equation

$$R=-(R_E+h_t)\cos\theta_{zen} +\sqrt{(R_E+h_t)^2\cos^2\theta_{zen}+2R_E(h_s-h_t)+h_s^2-h_t^2} \qquad (3.1.2)$$

where R_E is the Earth radius (6378 Km), h_t is the station height above sea level, h_s is the satellite altitude above sea level, and θ_{zen} is the zenith angle of the satellite as observed from the station. The zenith angle is the complement of the elevation angle E. In the following subsections, we will give further detail regarding the individual terms in the link equation.

3.2 Transmitter Gain

The transmitter in modern SLR systems is a modelocked laser which produces quasi-gaussian spatial and temporal profiles. The transmitter gain for a gaussian beam is given by the expression

$$G_t(\theta)=\frac{8}{\theta_t^2}\exp\left[-2\left(\frac{\theta}{\theta_t}\right)^2\right] \qquad (3.2.1)$$

where θ_t is the far field divergence half-angle between the beam center and the $1/e^2$ intensity point and θ is the beam pointing error. Typical values for θ_t in NASA systems fall between 50 and 75 microradians (10-15 arcseconds) which implies a transmitter gain in excess of $G_t = 1.4 \times 10^9$. As will be shown in Section 3.8, there is little motivation for choosing a beam divergence which is on the order of, or smaller, than the expected system tracking errors. As discussed in Section 3.9, atmospheric turbulence also sets a lower limit to the minimum beam divergence (and hence transmitter gain) that can be achieved.

In propagating through the mount optical system, the gaussian profile is usually radially truncated by some limiting aperture (e.g. the transmitter primary) and sometimes centrally obscured (e.g. by a secondary mirror in a Cassegrain telescope). Radial truncation of the gaussian beam produces weak secondary rings around a dominant central lobe in the far field. The central obscuration causes a transfer of energy from the central lobe to the outer rings. A general expression for the transmitter gain which accounts for both of these effects is given by

$$G_t=\frac{4\pi A_t}{\lambda^2}g_t(\alpha_t,\beta,\gamma_t,X) \qquad (3.2.2)$$

where $A_t=\pi a_t^2$ is the area of the transmitting aperture and $g_t(\alpha_t, \beta, \gamma_t, X)$ is a geometric factor [Klein and Degnan, 1974]. If the target is in the far field of the transmitter and the collimating telescope is perfectly focused (i.e., the exiting phasefronts are planar) then $\beta = 0$. Similarly, if there is no pointing error then $X = ka\sin\theta = 0$ where $k = 2\pi/\lambda$, and the on-axis gain is given by the simple expression

$$g_t(\alpha_t,0,\gamma_t,0)=\left(\frac{2}{\alpha_t^2}\right)\left(e^{-\alpha_t^2}-e^{-\gamma_t^2\alpha_t^2}\right) \qquad (3.2.3)$$

where $\alpha_t = a_t/w$ and $\gamma_t = b_t/a_t$ and a_t is the radius of the primary transmitting aperture, w is the gaussian beam waist radius at the transmitting primary, and b_t is the radius of an obscuring secondary mirror (if any). The choice of transmit primary radius to beam radius ratio, α_t, that maximizes the transmitter gain for an arbitrary obsuration ratio, α_t, has been shown to be [Klein and Degnan, 1974]

$$\alpha_t=1.12-1.30\gamma_t^2+2.12\gamma_t^4 \qquad (3.2.4)$$

for values of $\gamma_t < 0.4$. The optimum value of g_t is plotted versus the obscuration ratio γ_t in Figure 4. The transmitter gain is proportional to the inverse square of the wavelength in equation (3.2.2) which implies a higher degree of collimation for shorter wavelengths given a constant transmit aperture to beam radius ratio.

3.3 Effective Receiver Area

In a "bistatic" SLR system, the transmitting and receiving telescopes are not the same. An example is the NASA MOBLAS SLR system illustrated in Figure 5. To compute the effective receiver area, we must take into account the radiation lost to blockage by a secondary mirror (if any) and spillover at the spatial filter and/or detector (if any). The effective receiver area is given by the equation [Degnan and Klein, 1974]

Page06.jpg

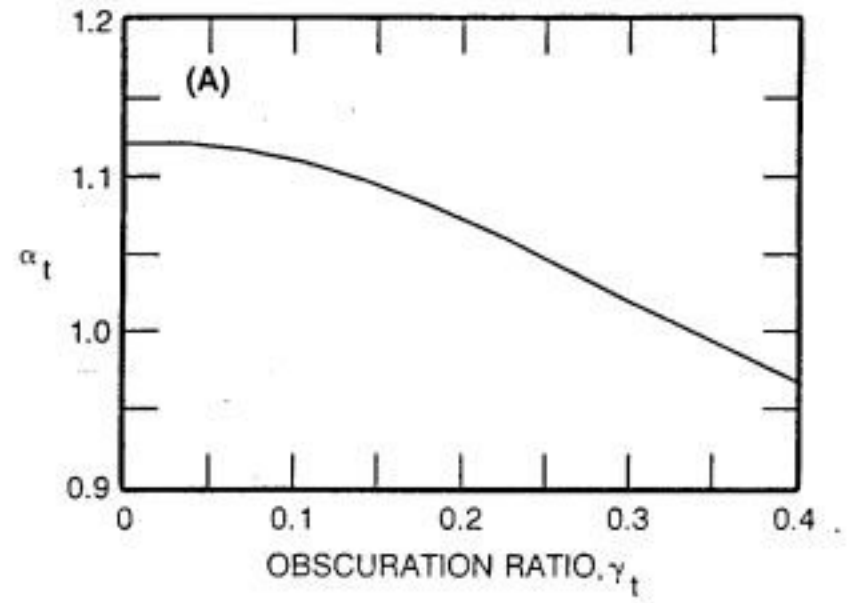

Fig. 4. (a) The ratio of the primary mirror radius to gaussian beam radius ($1/e^2$ intensity) which gives maximum far field gain as a function of the obscuration ratio, $\gamma_t = b/a$, defined as the ratio of the secondary mirror radius to the primary mirror radius. (b) The relative gain normalized to value $4\pi A/\lambda^2$.

$$A_r = A_p\left(1-\gamma_r^2\right)\eta_D\left(\gamma_r, \frac{kR_D}{2F_s}\right) \tag{3.3.1}$$

where $A_p = \pi a_r^2$ is the area of the receiver primary, $\gamma_r = b_r/a_r$ is the receiver obscuration ratio and $\left(1-\gamma_r^2\right)$ is the fraction lost due to blockage by the receiver secondary. The quantity

$$\eta_D\left(\gamma_r, \frac{kR_D}{2F_s}\right) = \frac{2}{1-\gamma_r^2}\int_0^{\frac{kR_D}{2F_s}}\left[J_1(u)-\gamma_r J_1(\gamma_r u)\right]^2\frac{du}{u} \tag{3.3.2}$$

is the fraction of the incoming light intercepted by a detector of radius R_D in the focal plane of a diffraction limited telescope. Alternatively, R_D could represent the radius of a pinhole aperture (spatial filter) in the focal plane of the receiver telescope.

In Equation (3.3.2), F_s is the F-number (focal length to diameter ratio) of the receiving telescope and $k = 2\pi/\lambda$ where λ is the wavelength. The quantity η_D is plotted in Figure 6 where individual curves are labelled by the obscuration ratio. The points of zero slope near $kR_D/2F_s = 3.5$ and 7.5 represent the first and second nulls of the modified Airy pattern respectively. Note that the central Airy lobe contains about 83% of the received energy for the unobscured case but only about 60% for $\gamma_r = 0.4$. For all obscurations, the central lobe and first Airy ring contain about 90% of the total energy incident on the receiver focal plane.

The detecting areas of conventional or microchannel plate photomultipliers are sufficiently large (15 to 18 mm diameter) that all of the incoming light, not blocked by the secondary, is collected ($\eta_D \sim 1$). However, this may not always be the case if the photomultiplier is replaced by a small (few hundred micron active aperture) high speed, avalanche photodiode or if a spatial filter is used during daylight ranging. From geometric optics, the half-angle of the receiver field of view in radians can be expressed in terms of the abscissa parameter in Figure 6, i.e.

$$\theta_r = \frac{R_D}{f} = \frac{1}{ka_r}\left(\frac{kR_D}{2F_s}\right) \tag{3.3.3}$$

where f is the telescope focal length. Expressed in steradians, the receiver field of view is

$$\Omega_r = \frac{\pi\theta_r^2}{4\pi} = \left(\frac{\theta_r}{2}\right)^2 \tag{3.3.4}$$

3.4 Atmospheric Attenuation

In the near-ultraviolet to visible spectral band between 0.3 and 0.7 μ, atmospheric attenuation is dominated by aerosol (Mie) scattering but molecular (Rayleigh) and ozone absorption also play a role [RCA, 1968]. In the near infrared beyond 0.7μ, the plot of atmospheric transmission versus wavelength (see Figure 7) is modulated by strong absorption features of various molecular constituents in the atmosphere, notably water vapor, oxygen, and carbon dioxide.

The transmission curve presented in Figure 7 corresponds to excellent "seeing" conditions (80 Km visibility) and 2 cm of precipitable water vapor. However, atmospheric seeing conditions vary widely from day to day and from site to site and are usually characterized by "sea level visibility" expressed in kilometers. Plots of the sea level attenuation coefficient versus wavelength (from 0.4 to 4μ) as a function of sea level visibility can be found in the RCA Electro-Optics Handbook [RCA, 1968]. The attenuation coefficient decreases approximately exponentially with height according to the equation

$$\sigma_{atm}(\lambda,V,h) = \sigma_{atm}(\lambda,V,0)\exp\left(-\frac{h}{h_{scale}}\right) \tag{3.4.1}$$

where $\sigma_{atm}(\lambda, V, h)$ is the attenuation coefficient at wavelength λ and altitude h for a sea level visibility of V, $\sigma_{atm}(\lambda, V, 0)$ is the value at sea level, and $h_{scale} = 1.2$ Km is a scale height. The one-way atmospheric transmission over a slant range to a satellite

Page07.jpg

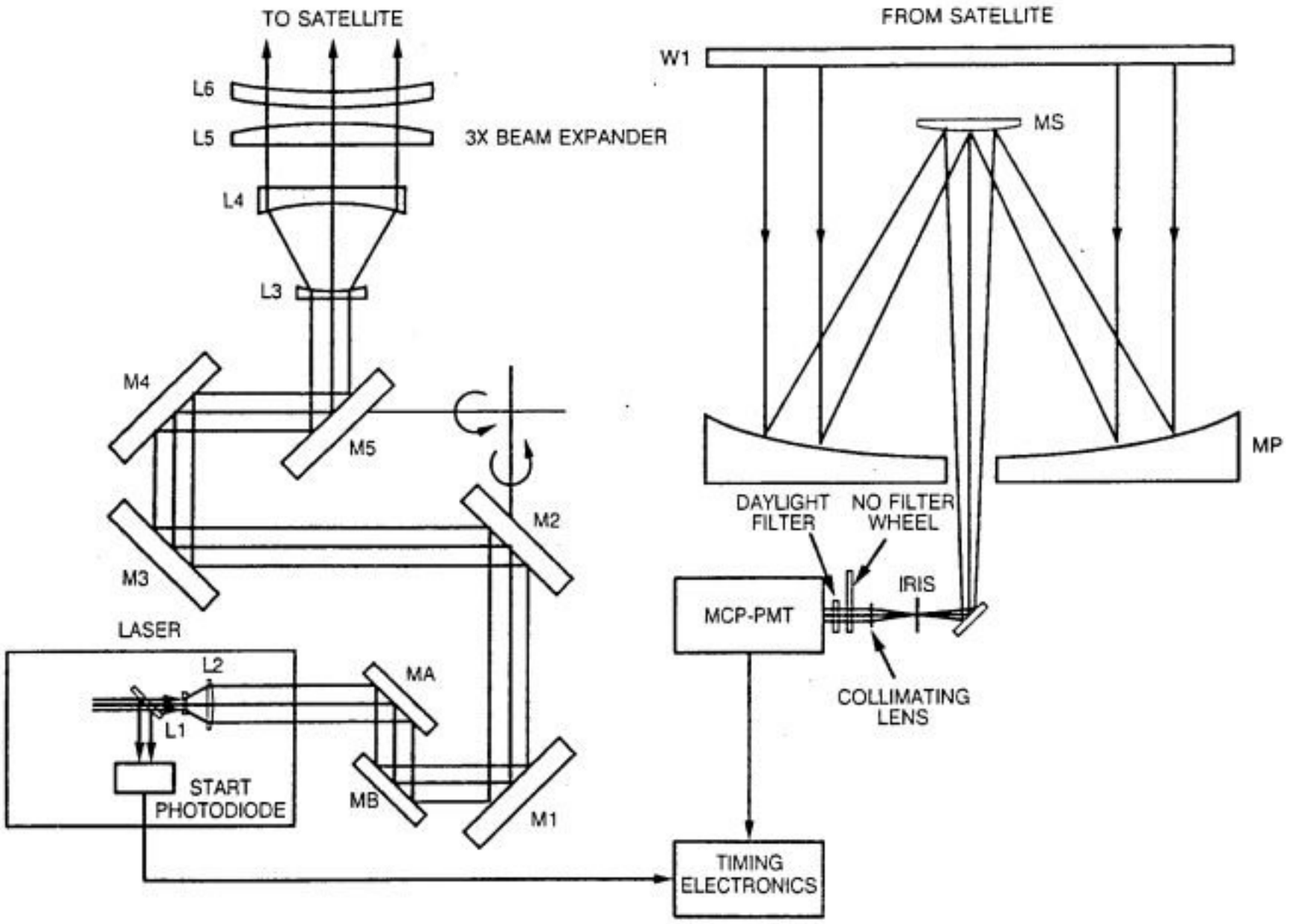

Fig. 5. MOBLAS optical schematic showing separate transmit receive optics.

from a site at an altitude h_t above sea level is then given approximately by

$$T_A(\lambda,V,h_t)=\exp\left[-\sec\theta_{zen}\int_{h_t}^{\infty}\sigma_{atm}(\lambda,V,h)dh\right]$$
$$=\exp\left[-\sigma_{atm}(\lambda,V,0)h_{scale}\sec\theta_{zen}\exp\left(-\frac{h_t}{h_{scale}}\right)\right] \quad (3.4.2)$$

where θ_{zen} is again the zenith angle of the satellite as observed at the station. In evaluating the integral in Eq.(3.4.2), we have assumed a straight line path and ignored the minor refractive bending of the ray in the atmosphere.

In plotting the two-way transmission at zenith for a station at sea level in Figure 8a, we have ignored the molecular line structure, so clearly visible in Figure 7, imposed by absorbing constituents such as water vapor, CO_2 and O_2. As can be seen from Figure 8b, the roundtrip atmospheric transmission at an elevation angle of 70° can decrease by over two orders of magnitude for UV wavelengths below 375 nm as one goes from extremely clear conditions (visibility > 60 Km) to light haze conditions (visibility ~8Km). The variation is less than one order of magnitude for near infrared wavelengths greater than 750 nm.

3.5 Cirrus Cloud Cover

The presence of thick cumulus clouds prevents ranging at optical wavelengths. However, even when skies appear relatively clear, sub-visible cirrus clouds are overhead about 50% of the time at most locations. A global study of cirrus cloud thickness [Hall et al., 1983] yields the histogram in Figure 9a. From the histogram, one can compute a mean cirrus cloud thickness, when present, of 1.341 Km.

For clouds with a total optical thickness (attenuation coefficient times cloud thickness) less than 0.5, very little wavelength dependence has been found over the wavelength range from 0.317 to 12 μ. Experimentally it is found that the cirrus transmittance is given by the equation

$$T_c=\exp[-.14(t\sec\theta_{zen})^2] \quad (3.5.1)$$

where t is the cirrus cloud thickness and θ_{zen} is the zenith angle. The cirrus cloud transmission is plotted as a function of cloud

Page08.jpg

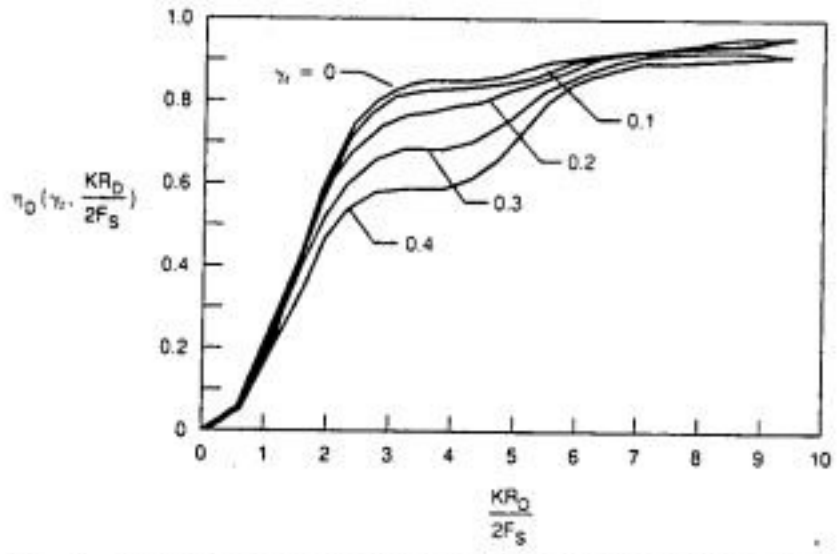

Fig. 6. Fraction of the radiation in the focal plane of the receiver intercepted by a detector of radius R_D or transmitted by a spatial filter of the same radius as a function of wavelength and receiver "F-number".

thickness for three different zenith angles - 0, 40, and 70 degrees - in Figure 9b. If one assumes the mean thickness, we obtain the curve in Figure 10. The cirrus transmission falls above the curve in Figure 10 about 75% of the time since, at a typical site, cirrus clouds are not present 50% of the time ($T_c = 1$), and, when they are present, their thickness is less than the mean value 50% of the time.

3.6 Background Noise and False Alarm Rate

The photoelectron generation rate resulting from background noise can be computed from the expression [Pratt, 1967]

$$\Lambda = \frac{\eta_q P_B}{h\nu} = \frac{\eta_q}{h\nu} N_\lambda (\delta\lambda) \Omega_r A_r \eta_r \qquad (3.6.1)$$

where η_q is the detector quantum efficiency, P_B is the background power entering the photodetector, $h\nu$ is the laser photon energy

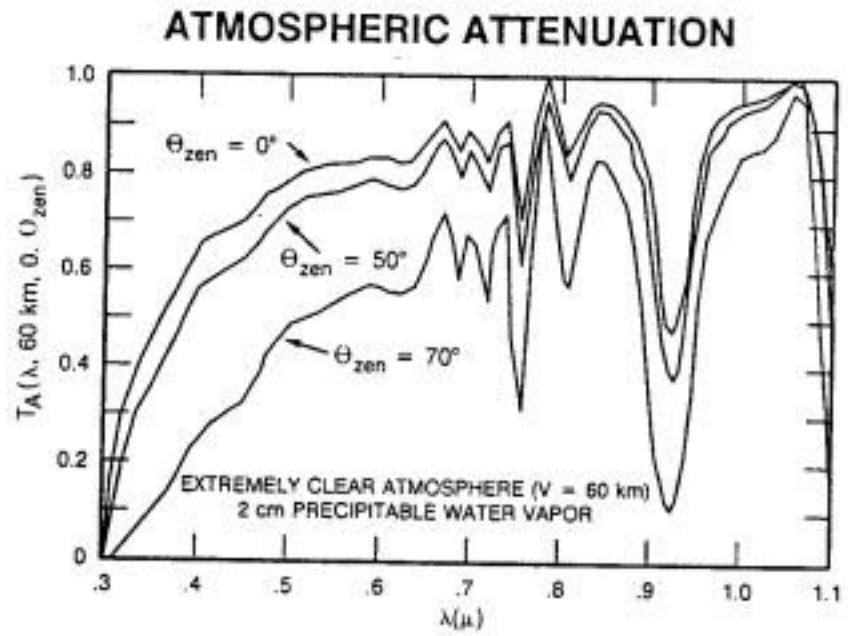

Fig. 7. Atmospheric transmission as a function of wavelength under extremely clear conditions with 2 cm of precipitable water vapor at zenith angles of 0, 50, and 70° (corresponding to 1, 2, and 3 air masses) respectively.

(coincides with the center of the receiver bandpass), N_λ is the background spectral radiance in units of Watts/m^2-A-ster, $\delta\lambda$ is the spectral width of the bandpass filter, Ω_r is the receiver field of view in steradians, and A_r and η_r are the effective receiver area and receiver optics efficiency discussed previously.

The probability of false alarm in the absence of a signal can be computed using the "sliding window integrator" model of a range receiver [McDonnell Douglas, 1977]. This yields the expression

$$P_{FA} = 1 - \exp\left[\frac{-\frac{(\Delta\tau_G)(\Delta\tau_r)^{n_t - 1}}{(n_t - 1)!}}{\sum_{m=0}^{n_t - 1} \frac{(\Delta\tau_r)^m}{m!}} \right] \qquad (3.6.2)$$

where τ_G is the temporal width of the range gate, and τ_r is the effective integration time (impulse response) of the receiver (~ 500 psec for the unamplified ITT 4129F microchannel plate photomultiplier used in NASA systems). The mean number of noise photoelectrons generated within the detector over a time frame equal to the receiver impulse response is given by

$$n_t = \Lambda\tau_r \qquad (3.6.3)$$

From equations (3.6.1) and (3.6.2), we see that the false alarm rate can be reduced in several ways, i.e. (1) reducing the width of the range gate τ_G (temporal filtering); (2) reducing the spectral width $\delta\lambda$ of the bandpass filter (spectral filtering); (3) reducing the receiver field of view Ω_r (spatial filtering); and/or (4) increasing the threshold setting n_t (amplitude filtering). Generally one chooses the threshold, n_t, to reduce the false alarm rate to an acceptable value after all other avenues for noise reduction have been exploited. The threshold can be adjusted via the threshold setting of the discriminator, a reduction in the photodetector gain, or a variable attenuator in the receiver path (best approach).

Generally, the spatial filter should be chosen such that the receiver field of view is slightly larger than that of the transmitter far field pattern, i.e. on the order of 200 microradians full angle or 2.5 x 10^{-9} steradians. The best commercially available narrowband spectral filters are (1) a 10 Angstrom filter with 70% transmission at the center wavelength and (2) a 3 Angstrom filter with 45% transmission at the center wavelength. Both have blocking densities on the order of 10^{-4} for out-of-band radiation. For high satellites with good orbit predictions such as LAGEOS, the range gate can be narrowed considerably (0.1 μsec < τ_G < 1 μsec) to further limit the influence of background noise. For low Earth orbiting satellites subject to large drag effects or frequent maneuvers, the range gate must sometimes be widened to several microseconds to accomodate a poorer range prediction. On the other hand, the higher signal levels associated with low satellites usually permit an increase in the effective threshold setting. In other words, temporal filtering can usually be traded off against amplitude filtering when ranging to low satellites in daylight.

As an illustration, we now perform a sample noise calculation for a NASA MOBLAS system. The diameters of the primary and

Page09.jpg

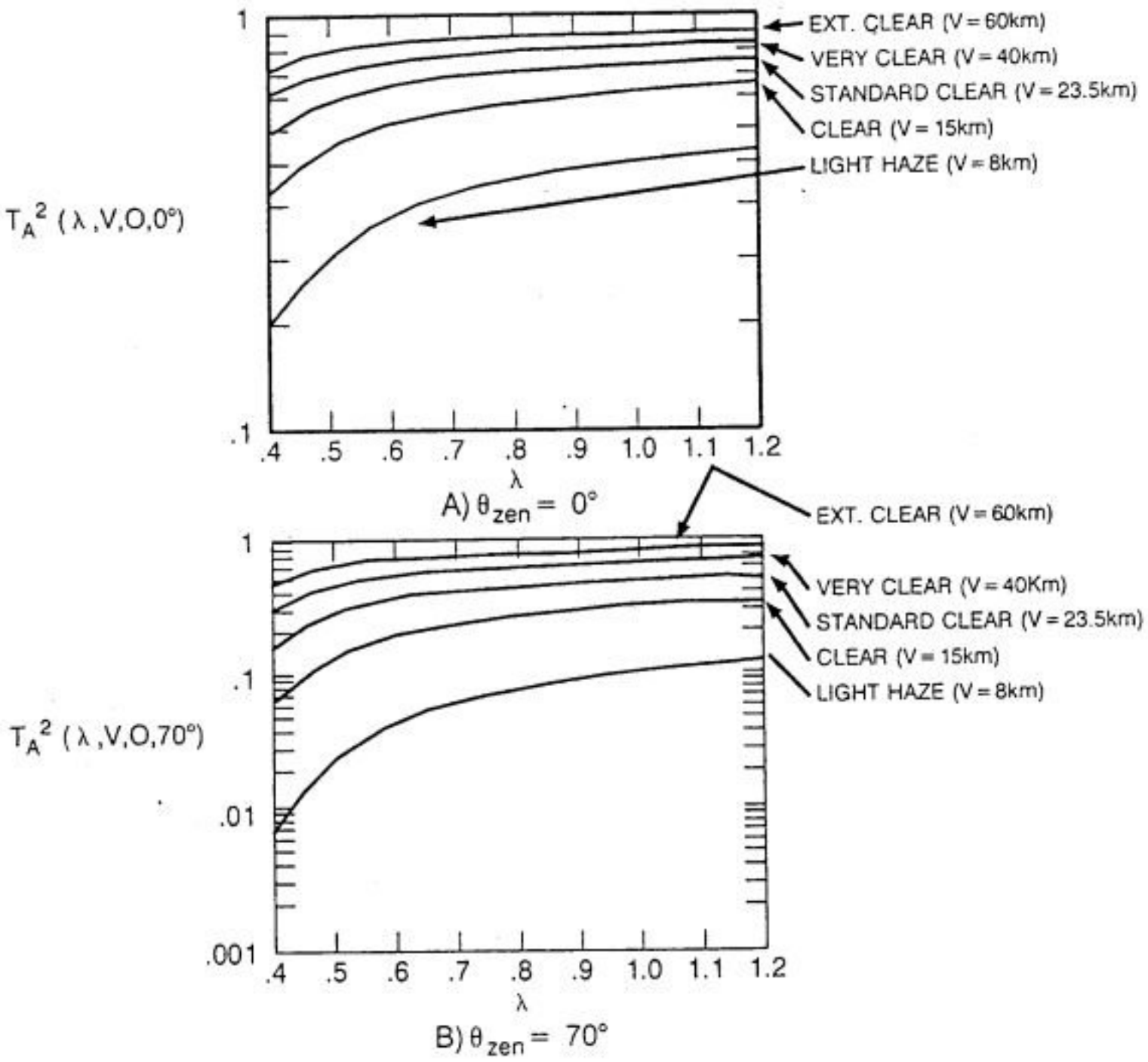

Fig. 8. Variation of the two-way atmospheric transmission with sea-level visibility at zenith angles of (a) 0° and (b) 70°.

secondary mirrors in the receiver telescope are 76.2 cm and 25.4 cm respectively resulting in an obscuration ratio $\gamma_r = 25.4/76.2 = 0.333$ and an effective receiver area of $A_r = 4055$ cm^2. At a wavelength of 532 nm, the photon energy is 3.73×10^{-19} Joules. In a MOBLAS, we typically have $\eta_q = .15$ for the detector quantum efficiency and $\delta\lambda = 10$ Angstroms, Ω_r is approximately 2.5×10^{-9} steradians for a slightly suboptimal 40 arcsecond (full angle) receiver field of view, and $\eta_r \sim 0.54$ (which includes a 30% loss in the daylight filter). Assuming the system does not look directly into the sun, sunlit clouds provide a worst case noise background of $N_\lambda = .014$ Watts/μ-ster-cm^2. Substituting these values into (3.6.1), we obtain a value $\Lambda = 3 \times 10^7$/sec for the photoelectron rate due to background noise. The resulting average background noise count within the receiver impulse response of 500 psec, $\Lambda\tau_r$, is only .015 photoelectrons, but the photoelectron noise count within a typical one microsecond range gate, $\Lambda\tau_G$, is 30. Substituting different threshold values into (3.6.2), we obtain the results in Table 1, which indicate that, for a one microsecond range gate, a threshold of 3 photoelectrons gives a perfectly acceptable probability of false alarm for daylight ranging even in the presence of sunlit clouds. This is in good agreement with actual MOBLAS settings.

3.7 Probability of Detection

The detection of photoelectrons follows Poisson statistics. If $n = n_s + n_b$ is the sum of the mean number of signal and noise photoelectrons within the detector impulse response, the probability of detecting m photoelectrons is given by the equation

$$P(m,n) = \frac{n^m}{m!} e^{-n} \tag{3.7.1}$$

Page10.jpg

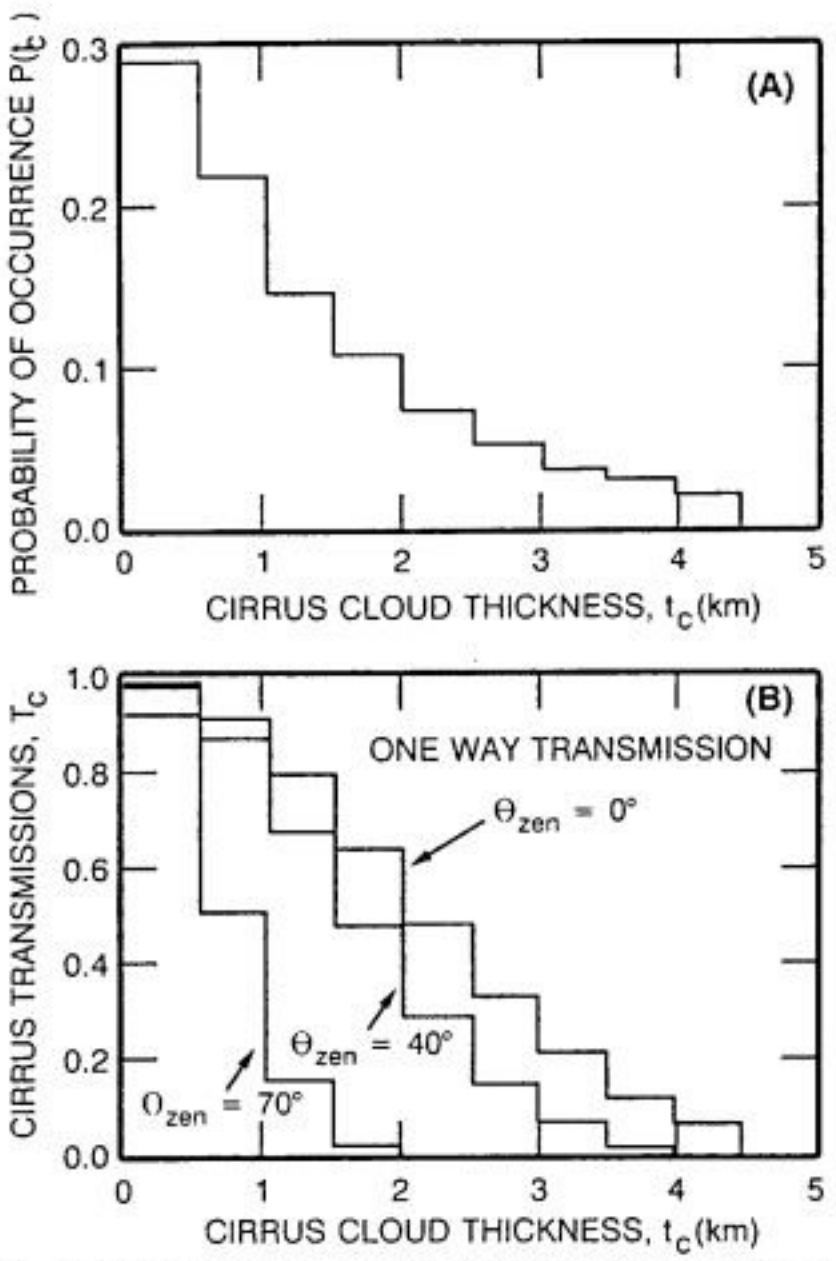

Fig. 9. (a) Probability of occurrence of cirrus clouds having thickness t_c when cirrus clouds are present. (b) One way transmission as a function of cirrus cloud thickness.

Equation (3.7.1) makes the assumption (valid for third generation SLR systems ranging to geodetic satellites such as STARLETTE and LAGEOS) that the pulse waveform returning from the satellite is short in duration compared to the receiver impulse response. The probability of detection is then equal to the probability that the number of photoelectrons detected (signal plus noise) exceeds the threshold value, n_t. Thus,

$$P_D(n,n_t)=1-e^{-n}\sum_{m=0}^{m=n_t-1}\frac{n^m}{m!} \qquad (3.7.2)$$

Using the daylight threshold value determined in Section 3.8 ($n_t = 3$), we obtain a plot of the probability of detection versus mean signal level in Figure 11. We see that the probability of detection is 60% for mean signals at the threshold value and is essentially unity for signal levels in excess of 10 photoelectrons.

Using the link equation and graphs from the previous subsections, we can construct the following table to compute the maximum and minimum signal levels for a MOBLAS station

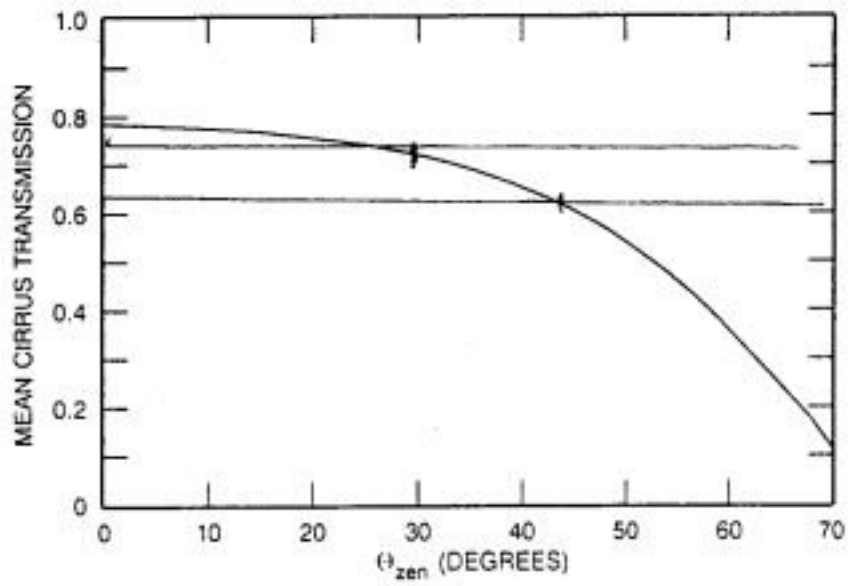

Fig. 10. Mean cirrus transmission (one-way) as a function of zenith angle. The one-way transmission falls above the curve 75% of the time and below the curve 25% of the time under the assumption that cirrus clouds are present only 50% of the time at a given location.

ranging to LAGEOS under "best" and "worst" case conditions. The calculations do not include the effects of pointing errors or atmospheric turbulence which will be discussed in the next two subsections. We see from Table 2 that the signal levels to LAGEOS can vary by over four orders of magnitude. Almost two orders of magnitude can be attributed to variations in the atmospheric transmission as a function of sea level visibility and elevation angle. An additional order of magnitude is contributed by mean cirrus cloud cover at low elevation angles, while the rest of the difference is due to variations in slant range and hardware characteristics or settings.

For the NASA TLRS 1, 3, and 4 systems, the received photoelectrons would be reduced by roughly a factor of ten relative to a MOBLAS (i.e. $61 > n_{pe} > .005$) because of the smaller receiver aperture (28 cm vs 76 cm). Since the NASA TLRS-2 system has both a smaller receive aperture (26 cm) and emits a factor of 10 less energy (10 mJ), its mean number of received photoelectrons would fall in the range $6 > n_{pe} > .0005$.

3.8 Pointing Errors

The calculations of Section 3.7 assume there is no transmitter pointing error. In considering pointing error, it is easiest to work with the gaussian transmitter far field pattern given by Eq.(3.2.1).

TABLE 1. Probability of False Alarm as a Function of Detection Threshold for a MOBLAS Station Operating in the Presence of Sunlit Clouds with a One Microsecond Range Gate

Threshold (pe)	Prob. False Alarm
1	1.000
2	0.360
3	0.002

Page11.jpg

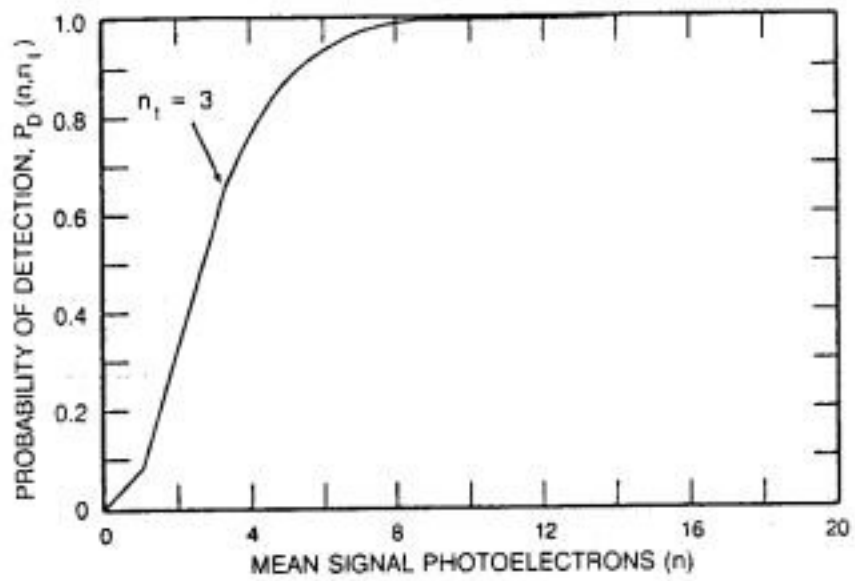

Fig. 11. Probability of detection as a function of mean signal photoelectron level for a 3 photoelectron detection threshold.

Even in the presence of truncation and central obscuration of the transmit beam, a gaussian can be fit reasonably well near the center of the central far field lobe.

Let us assume that α is the pointing bias in azimuth, β is the pointing bias in elevation, $\delta\alpha$ is the instantaneous random error in azimuth, and $\delta\beta$ is the instantaneous random error in elevation. Then the mean signal level is

$$\langle n_s\rangle = n_s\int_{-\infty}^{\infty} d(\delta\alpha)P(\delta\alpha)\cdot \int_{-\infty}^{\infty} d(\delta\beta)P(\delta\beta)\exp\left[-2\left(\frac{\alpha+\delta\alpha+\beta+\delta\beta}{\sigma_t}\right)^2\right] \tag{3.8.1}$$

where n_s is the mean signal with no pointing error, σ_t is the transmitter divergence half angle θ_t defined previously in Section 3.2, and $P(\delta\alpha)$ and $P(\delta\beta)$ are the probability distributions for the random pointing errors in the two axes. If we make the assumption that the two probability functions are also gaussian, e.g.

$$P(\delta\alpha) = \sqrt{\frac{2}{\pi}}\frac{1}{\sigma_\alpha}\exp\left(-2\left(\frac{\delta\alpha}{\sigma_\alpha}\right)^2\right) \tag{3.8.2a}$$

$$P(\delta\beta) = \sqrt{\frac{2}{\pi}}\frac{1}{\sigma_\beta}\exp\left(-2\left(\frac{\delta\beta}{\sigma_\beta}\right)^2\right) \tag{3.8.2b}$$

the resulting integrals can all be evaluated analytically. This yields the following expression for the mean signal in the presence of a fixed pointing bias and random pointing errors

$$\langle n_s\rangle = n_s\frac{\sigma_{t\alpha}\sigma_{t\beta}}{\sigma_\alpha\sigma_\beta}\exp\left[-2\left(\frac{\alpha^2+\beta^2}{\sigma_t^2}\right)\right]\exp\left[\frac{2}{\sigma_t^4}\left(\alpha^2\sigma_{t\alpha}^2+\beta^2\sigma_{t\beta}^2\right)\right] \tag{3.8.3}$$

where we have defined

$$\frac{1}{\sigma_{t\alpha}^2} = \frac{1}{\sigma_t^2}+\frac{1}{\sigma_\alpha^2} \tag{3.8.4a}$$

and

$$\frac{1}{\sigma_{t\beta}^2} = \frac{1}{\sigma_t^2}+\frac{1}{\sigma_\beta^2} \tag{3.8.4b}$$

In the absence of a pointing bias, i.e $\alpha = \beta = 0$, (3.8.3) for the mean signal reduces to the much simpler expression

$$\langle n_s\rangle = n_s\frac{\sigma_{t\alpha}\sigma_{t\beta}}{\sigma_\alpha\sigma_\beta} \tag{3.8.5}$$

If the probability distribution is the same for both mount axes ($\sigma_\alpha = \sigma_\beta = \sigma_p$), (3.8.5) becomes simpler still, i.e.

$$\langle n_s\rangle = n_s\frac{\sigma_{tp}^2}{\sigma_p^2} = n_s\frac{1}{1+\dfrac{\sigma_p^2}{\sigma_t^2}} \tag{3.8.6}$$

Higher order moments of the signal distribution are easily computed by noting that the expectation value of the mth power of signal $\langle n_s^m\rangle$ can be computed by replacing n_s by n_s^m and replacing σ_t by $\sigma_t/\sqrt{m}$ in all of the previous equations of this section. Thus, for the especially simple case of no pointing bias and equal pointing variances in the two mount axes, the variance

TABLE 2. "Best" and "Worst" Case Signal Levels for a MOBLAS Station Ranging to LAGEOS

Parameter	Maximum	Minimum
Detector Quantum Efficiency, η_q	0.18	0.10
Photons Transmitted, $E\lambda/hc$	2.7×10^{17} (100 mJ)	1.6×10^{17} (60 mJ)
Trans. Optics Eff., η_t	.66	.66
Transmitter Gain, G_t	3.2×10^8 (20 arcsec)	1.4×10^9 (30 arcsec)
Satellite Cross-section, σ	7×10^6 m^2 LAGEOS	7×10^6 m^2 LAGEOS
Two Way Space Loss, $(1/4\pi R^2)^2$	4.9×10^{-30} m^{-4} LAGEOS, E = 90° R = 6000 Km	1.1×10^{-30} m^{-4} LAGEOS, E = 20° R = 8649 Km
Receiver Area, A_r	0.4055 m^2	0.4055 m^2
Receive Optics Eff., η_r	0.54	.054
Two-Way Atmospheric Transmission T_a^2	0.8 Ex. Clear E = 90°	0.02 Lt. Haze E = 20°
Two-Way Cirrus Transmission, T_c^2	1.0 No Cirrus	0.1 Mean Cirrus E = 20°
Received Photoelectrons, N_{pe}	612	0.05

Page12.jpg

in the signal level produced by random pointing errors can be easily shown to be

$$\langle (n_s - \langle n_s \rangle)^2 \rangle = \langle n_s^2 \rangle - \langle n_s \rangle^2 = n_s^2 \left[\frac{1}{1 + \frac{2\sigma_p^2}{\sigma_t^2}} - \left(\frac{1}{1 + \frac{\sigma_p^2}{\sigma_t^2}} \right)^2 \right] \quad (3.8.7)$$

The mean and RMS standard deviation (square root of variance) of the signal level distribution, normalized to the mean signal in the presence of no pointing error, is plotted as a function of σ_p/σ_t in Figure 12. For pointing variances on the order of the transmitter beamwidth, the typical signal range is $(0.5 \pm 0.3)\ n_s$ for a system with no angular bias. When the RMS tracking jitter is much smaller than the angular transmitter beamwidth ($<20\%$), the signal reduction due to pointing errors is relatively small.

3.9 Atmospheric Turbulence

The total effect of atmospheric turbulence on laser beam propagation is a highly complex subject, and a full accounting of the theoretical and experimental work in this area is beyond the scope of the present review. For more detail on electromagnetic beam propagation in the turbulent atmosphere, the reader is referred to two excellent early reviews of the subject by Fante [1975, 1980]. An up-to-date and comprehensive review of all aspects of optical beam propagation in the atmospheric channel can be found in the book by Karp et al. [1988] who apply the results to an analysis of optical communications systems. In addition, Ricklin [1990] has reviewed the theory as it relates to gaussian beam propagation and has presented many numerical results. Most recently, Churnside [1992] has surveyed the available literature and applied it to the spaceborne Geoscience Laser Ranging System proposed by Cohen et al. [1987].

Random spatial variations in the atmospheric refractive index result in a distortion of the spatial phasefronts of propagating

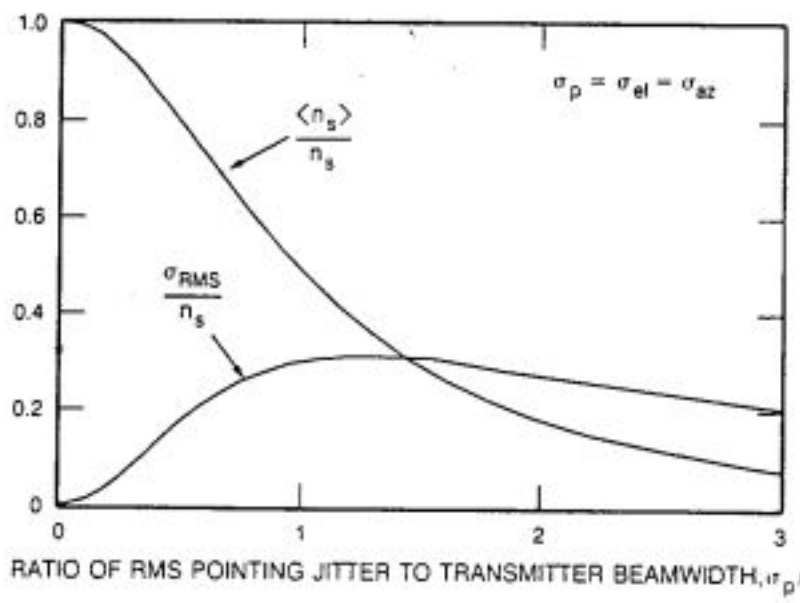

Fig. 12. Plot of the normalized mean signal level and RMS standard deviation versus the ratio of the RMS pointing jitter to transmitter beamwidth. The mean and RMS standard deviation are normalized to the mean signal level, n_s, in the absence of pointing errors.

electromagnetic beams. A primary source of these index variations is the turbulent motion of the atmosphere in the presence of temperature and moisture gradients. This "optically turbulent" atmosphere produces three effects on low power laser beams: (1) beam wander, (2) beam spread and (3) scintillation. Severe optical turbulence can result in total beam breakup [Ricklin, 1990]. Fante [1975] has presented calculations which suggest that pulse broadening and distortion effects, due to the dispersion in a turbulent atmosphere, can typically be ignored for all but the shortest pulsewidths (few picoseconds) and hence will not be considered further here.

"Beam wander" refers to random translations of the spatial centroid of the beam and is generally caused by the larger turbulent eddies through which the beam passes. "Beam spread" is a short term growth in the effective divergence of the beam produced by smaller eddies in the beam path. The two effects are often discussed together in terms of a "long term" and "short term" beam spread. The "long term" beam spread includes the effects of beam wander whereas the "short term" beam spread does not. It can be shown, by manipulating the results of Fante [1975], that the long term divergence angle for an initially collimated gaussian beam is given by

$$\langle \theta_L \rangle = \left(\frac{\langle \rho_L^2 \rangle}{R^2} \right)^{1/2} = \theta_t \sqrt{1 + \left(\frac{w_o}{\rho_o} \right)^2} \quad (3.9.1)$$

where w_o is the effective gaussian beam waist radius defined as the radius to the $1/e^2$ intensity point and $\theta_t = \lambda/\pi w_o$ is the turbulence-free beam divergence introduced in Section 3.2. The transverse atmospheric coherence length, ρ_o, is defined by

$$\rho_o = \left[1.46 k^2 R \int_0^1 d\xi (1-\xi)^{5/3} C_n^2(\xi R) \right]^{-3/5} \quad (3.9.2)$$

where $k = 2\pi/\lambda$, R is the slant range to the target and the variable $\xi = s/R$ is the normalized distance along the slant path to the target. The atmospheric structure constant, $C_n^2(h)$, is a measure of the magnitude of the fluctuations in the index of refraction and, as we shall soon see, falls off rapidly with altitude, h.

Since, for the uplink to the satellite, the atmosphere is concentrated in the region where $\xi \sim 0$, the integral in (3.9.2) is well approximated by

$$\rho_o = \left[1.46 k^2 \sec\theta_{zen} \int_{h_o}^{\infty} dh C_n^2(h) \right]^{-3/5} \quad (3.9.3)$$

where h_o is the height of the emerging laser beam. For the downlink from the satellite to the ground, $\xi \sim 1$ in the segment of the path which lies in the atmosphere and therefore the downlink contribution to beam spreading is small compared to that of the uplink [Churnside, 1992].

Fante [1975] has also provided expressions from which the short term beam spread and the variance in centroid shift in pointing

Page13.jpg

angle space can be derived. The short term spread for an initially collimated gaussian beam is

$$\langle\theta_s\rangle=\left(\frac{\langle\rho_L^2\rangle}{R^2}\right)^{1/2}=\left(\frac{\lambda}{\pi w_o}\right)\left\{1+(w_o/\rho_o)^2\left[1-0.62\left(\frac{\rho_o}{w_o}\right)^{1/3}\right]^{6/5}\right\}^{1/2} \quad (3.9.4)$$

and the variance in centroid shift is

$$\langle\theta_c^2\rangle=\frac{\langle\rho_c^2\rangle}{R^2}=\frac{2.97}{k^2\rho_o^{5/3}w_o^{1/3}} \quad (3.9.5)$$

Figure 13 provides a plot of the long and short term transmitter beam spread as a function of the coherence length. The curves are normalized to the transmitter divergence in the absence of turbulence as defined by (3.2.1). If one has a means of computing the coherence length, the effect of turbulence-induced beam spreading on mean signal level can be immediately obtained using (3.2.1) and Figure 13.

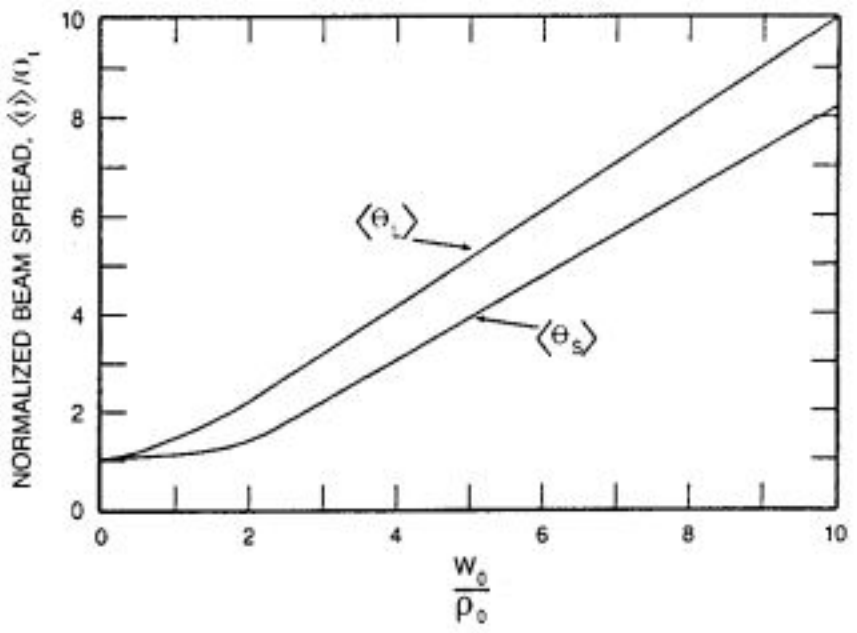

Fig. 13. Turbulence-induced long and short term gaussian beam spread as a function of the ratio of the transmitter gaussian beam waist radius, w_o, to the transverse coherence length, ρ_o . The curves are normalized to the transmitter divergence in the absence of atmospheric turbulence.

In order to compute the coherence length from (3.9.3), it is necessary to know the height dependence of the structure constant. Various models have been proposed [Hufnagel, 1974; Walters and Kunkel, 1981; Sasiela, 1988]. Walters and Kunkel [1981] based their model on data collected (via ground, tower, and aircraft measurements) over a 1.3 year period at desert and mountaintop sites. The dependence of $C_n^2(h)$ on altitude is given by [Walters and Kunkel, 1981]

$$C_n^2(h_o)\left(\frac{h}{h_o}\right)^{-4/3} \qquad h_a<h<0.5h_{inv}$$

$$C_n^2(h_o)\left(.5\frac{h_{inv}}{h_o}\right)^{-4/3} \qquad 0.5h_{inv}<h<0.7h_{inv} \quad (3.9.6)$$

$$2.9C_n^2(h_o)\left(.5\frac{h_{inv}}{h_o}\right)^{-4/3}\left(\frac{h}{h_{inv}}\right)^{3} \qquad 0.7h_{inv}<h<h_{inv}$$

where h_a is the site height above the surface from which laser beam propagation begins, h_{inv} (~1 to 2 Km) is the height of the inversion layer, h_{lim} (~20 Km) is the upper limit of the atmosphere, and $C_n^2(h_o)$ is the value of the structure constant at the reference height, h_o. The contribution of the atmosphere lying above the inversion layer is relatively constant and can be approximated by

$$\int_{h_{inv}}^{h_{lim}}dhC_n^2(h)=2.36\frac{\left(1-\frac{h_{inv}}{h_{lim}}\right)}{k_{ref}^2\rho_{o\,ref}^{5/3}}\left(\frac{k_{ref}}{k}\right)^2=\frac{109m^{1/3}}{k^2}\left(1-\frac{h_{inv}}{h_{lim}}\right) \quad (3.9.7)$$

where we have used the value $\rho_{o\,ref}$ = 0.1 m for the reference wavelength at 500 nm [Walters and Kunkel, 1981]. Substituting (3.9.6) and (3.9.7) into (3.9.3) and performing the integrals yields an analytic expression for the coherence length, i.e.

$$\rho_o^{-5/3}=1.46k^2\sec\theta_{zen}\cdot\left\{h_oC_n^2(h_o)\left[3\left(\frac{h_o}{h_a}\right)^{1/3}-1.90\left(\frac{h_o}{h_{inv}}\right)^{1/3}\right]+\frac{109m^{-5/3}}{k^2}\left(1-\frac{h_{inv}}{h_{lim}}\right)\right\} \quad (3.9.8)$$

where the first two terms in brackets give the contribution of the atmosphere below the inversion layer and the last term gives the contribution of the atmosphere above the inversion layer.

To assess the maximum impact of turbulence-induced beam spreading on SLR signal level, we now consider a worst case situation. Maximum turbulence occurs at mid-day in the desert under clear weather conditions. The average mid-day value of $C_n^2(h_o)$ over Tularosa Basin during the months of April 1977 to July 1978 was observed to be 7.7 x 10^{-13} $m^{-2/3}$ at a reference height h_o = 1m [Walters and Kunkel, 1981]. If we assume the usual laser wavelength of 532 nm, a relatively high h_{inv} equal to 2 Km, and a relatively low system height equal to the reference height (1m), one obtains worst case values of 4.6 and 2.4 cm for the coherence length at zenith angles of 0° and 70° respectively. At the tripled Nd:YAG wavelength (355 nm), the corresponding values are 3.1 and 1.6 cm. From Figure 13, we see that turbulence-induced beam spreading will only have a significant impact on beam divergence (and hence signal level) if the coherence length is on the order of, or smaller than, the original effective beam waist radius. Since a typical 150 microradian beam implies an effective waist radius of 2.26 mm, the effect of beam spread on signal level for such systems is relatively small, i.e. a few percent. One can also see from (3.9.1) that, as the

Page14.jpg

beam radius w_o becomes large, the coherence length imposes a limiting divergence given by

$$\theta_{min} = \frac{\lambda}{\pi \rho_o} \tag{3.9.9}$$

which is plotted in Figure 14. For the strong turbulence case just considered, θ_{min} is about 7 microradians or 1.4 arcseconds (2.8 arcseconds full angle between $1/e^2$ intensity points) for a zenith angle of 70° and a wavelength of 532 nm.

Scintillation or "beam fading" is responsible for the familiar "twinkling" of starlight. Atmospheric turbulence produces a fluctuation in the received intensity at a point detector. In the limit of weak turbulence, it leads to a log-normal probability distribution for the received photoelectron count given by [Ochs and Lawrence, 1969]

$$P(I) = \frac{1}{\sqrt{2\pi}\,\sigma I} \exp\left\{-\left(\ln I + \frac{\sigma^2}{2}\right)^2 / 2\sigma^2\right\} \tag{3.9.10a}$$

where

$$\sigma^2 = 1 + \sigma_I^2 \tag{3.9.10b}$$

and σ_I is the normalized variance of the intensity fluctuations over a small (point) receiver aperture. Aperture averaging, which occurs at both the target retroreflectors and at the ground receiving telescope, tends to reduce the magnitude of the fluctuations [Fante, 1975]. Thus, the round trip propagation geometry must be considered when evaluating theoretical scintillation levels. This is a nontrivial computation which we will leave for others but, for the general case, we can expect the effects of scintillation to be significant under conditions of strong turbulence [Churnside, 1992].

Turbulence also introduces a random component to the atmospheric delay. The RMS path deviation depends on the refractive index structure constant C_{no}^2 which varies with time of day. For the von Karman spectral model of atmospheric turbulence, the theoretical RMS path deviation is given by [Gardner, 1976]

$$\sigma_{atr}^2 = 3.13 C_{no}^2 L_o^{5/3} h_{atr} / \cos\theta_{zen} \tag{3.9.11}$$

where L_o is the outer scale of turbulence ($L_o \sim 100$ m for satellite ranging [Lutz et al., 1983]), h_{atr} (~ 3 Km) is the atmospheric scale height for turbulence, and θ_{zen} is the zenith angle. Under low turbulence conditions (such as at night), σ_{atr} is submillimeter for elevation angles above 20°, but, under conditions of strong turbulence, it can approach a few millimeters [Lutz et al., 1983].

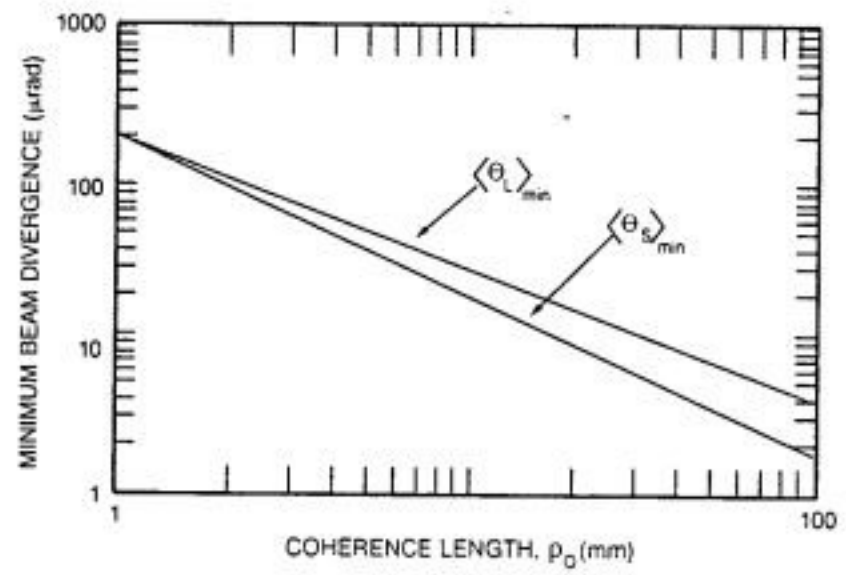

Fig. 14. Minimum long and short term gaussian beam divergence in the presence of turbulence.

4. Atmospheric Refraction

Of the three principal space geodetic techniques presently utilized by NASA (i.e. SLR, VLBI, and GPS), SLR suffers the least from propagation variabilities in the atmospheric channel. Compared to the microwave frequencies utilized by the VLBI and GPS techniques, SLR optical frequencies are relatively insensitive to the two most dynamic (and hence least predictable) components of the atmospheric propagation delay, i.e. the ionosphere and water vapor distribution. Ions are too heavy and sluggish to respond to optical frequencies in the 300 to 900 Terahertz range, and laser wavelengths in the visible and near ultraviolet are typically far from strong absorption features in the water vapor spectrum. Specifically, the effect of water vapor on laser ranges is roughly 70 times smaller than for microwave distance measurements [Hauser, 1989]. Thus, the so-called "dry" component of the atmosphere is the principal contributor to the propagation error in SLR.

4.1 Spherical Shell Models

As the laser pulse traverses the atmosphere, it sees a varying refractive index resulting primarily from spatial variations in the local density. The varying refractive index influences the propagating pulse in two ways. The dominant effect from a laser ranging standpoint is the variation of group velocity with atmospheric density, i.e. the pulse speeds up as it travels from the ground station through lower density regions at higher altitudes. The second, and smaller, effect is a consequence of Snell's law of refraction which predicts that the light ray will follow a curved, rather than straight, path as it moves between atmospheric "layers" having different refractive indices.

The atmospheric model traditionally used by the SLR community in modelling and correcting for atmospheric propagation delays in single color SLR systems is one originally developed almost two decades ago [Marini and Murray, 1973]. The Marini-Murray model is one of several models which assume that the atmosphere is composed of a series of infinitesimally thin spherically symmetric shells. Under this assumption, the ray path conveniently lies entirely in a plane, as in Figure 15. The "apparent" range, or optical path length, measured by a pulsed laser system is then given by

Page15.jpg

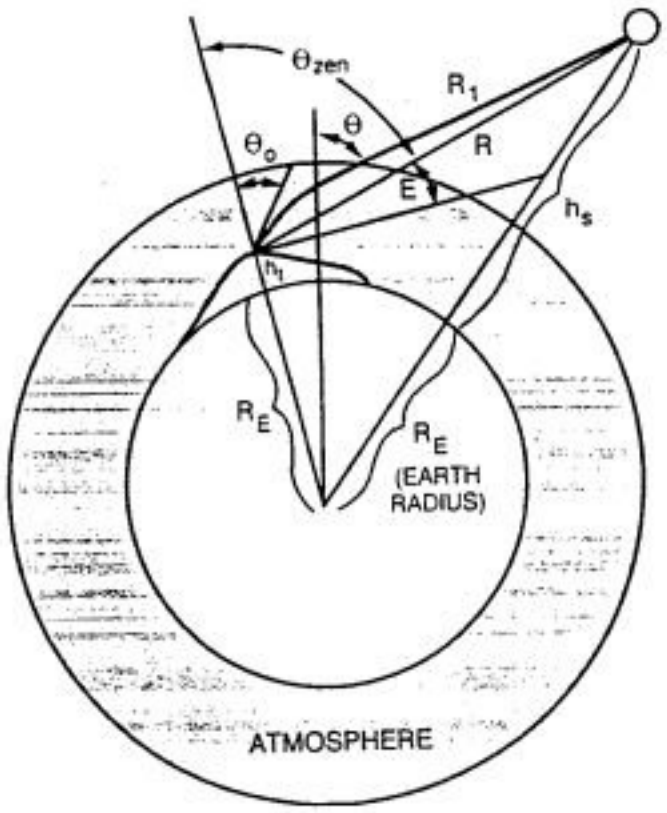

Fig. 15. Coordinate system used in the discussion of atmospheric refraction and the spherical shell model.

$$R' = \int_{r_o}^{r_1} dr \frac{n_g}{\cos\theta} \tag{4.1.1}$$

where n_g is the group index of refraction and the angle θ at an arbitrary point along the path is given by Snell's law for a spherically stratified medium, i.e.

$$nr\sin\theta = n_o r_o \sin\theta_o \tag{4.1.2}$$

where n_o is the refractive index at the surface. The atmospheric refraction correction is simply the difference between (4.1.1) and the geometric range, R, and can be written in the form

$$AC = R' - R = 10^{-6}\int_{r_o}^{r_1} dr \frac{N_g}{\cos\theta} + \left[\int_{r_o}^{r_1} \frac{dr}{\cos\theta} - R\right] \tag{4.1.3}$$

where

$$n_g = 1 + 10^{-6} N_g \tag{4.1.4}$$

and N_g is the group refractivity. The first term in (4.1.3) corresponds to the group velocity effect and the second term is the difference between the curved and straight ray paths.

4.2 Marini-Murray Model

The expression for N_g used by Marini and Murray is [IAG, 1963]

$$N_g(\lambda) = 80.343 f(\lambda)\frac{P}{T} - 11.3\frac{e}{T} \tag{4.2.1}$$

where P, T, and e are the local pressure (mbar), temperature (°K), and water vapor partial pressure (mbar) respectively. Note that the latter term assumes no dependence of the water vapor term on wavelength.

In the Marini-Murray model of the atmosphere [Marini and Murray, 1973], radial variability in the meteorological parameters (i.e. with altitude) is assumed to be governed by the equations for hydrostatic equilibrium, the law of partial pressures, and the perfect gas law. This leads to the following equations for the spherical range correction, SC_{MM}:

$$SC_{MM}(\lambda, E, P_H, T_H, e_H) = \frac{f(\lambda)}{F(\phi,H)} \frac{A(P_H, e_H) + B(\phi, T_H, P_H)}{\sin(E) + \dfrac{B(\phi, T_H, P_H)}{\dfrac{A(P_H, e_H) + B(\phi, T_H, P_H)}{\sin E + .01}}} \tag{4.2.2}$$

where

$$f(\lambda) = .9650 + \frac{.0164}{\lambda^2} + \frac{.000228}{\lambda^4} \tag{4.2.2a}$$

$$F(\phi,H) = 1 - .0026\cos 2\phi - .00031H \tag{4.2.2b}$$

$$A(P_H, e_H) = .002357 P_H + .000141 e_H \tag{4.2.2c}$$

$$B(\phi, T_H, P_H) = 1.084\times10^{-8} P_H T_H K(\phi, T_H, P_H) + 4.734\times10^{-8}\frac{P_H^2}{T_H}\frac{2}{3 - \dfrac{1}{K(\phi, T_H, P_H)}} \tag{4.2.2d}$$

and

$$K(\phi, T_H, P_H) = 1.163 - .00968\cos 2\phi - .00104 T_H + .00001435 P_H \tag{4.2.2e}$$

where λ is the laser wavelength in microns, E is the true elevation angle of the satellite in degrees, ϕ is the station latitude, H is the station height above mean sea level, and P_H (mbar), T_H (°K), and e_H (mbar) are the surface pressure, temperature, and water vapor pressure at the station. The water vapor pressure e_H is related to

Page16.jpg

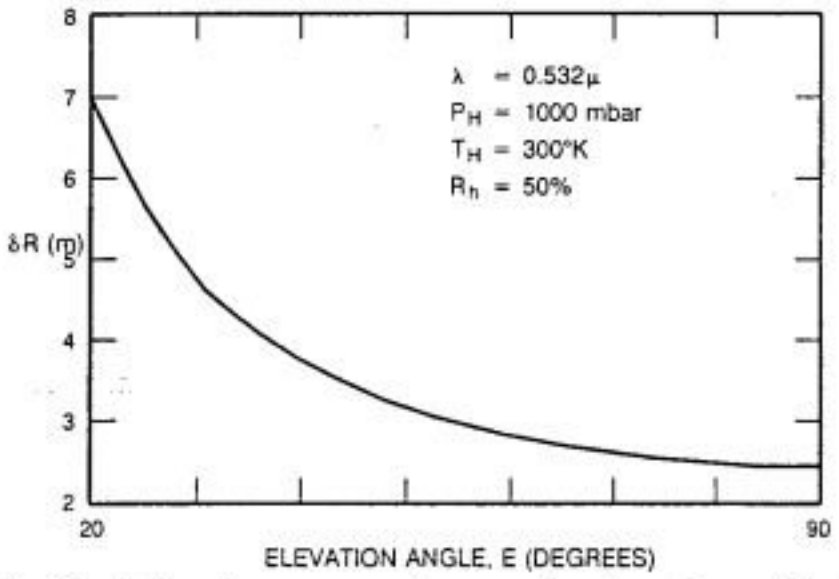

Fig. 16. Single color range correction versus elevation angle as predicted by the Marini-Murray spherical shell model for a wavelength of 532 nm and nominal surface meteorological parameters.

the surface percent relative humidity R_H and surface temperature T_H by the equation

$$e_H(R_H,T_H)=\frac{R_H}{100}6.11x10^{\left(7.5\frac{T_H-273.15}{237.3+(T_H-273.15)}\right)} \qquad (4.2.3)$$

The wavelength dependence of the range correction is contained in the dispersion term $f(\lambda)$. It was arbitrarily chosen to have a value of unity at the ruby laser wavelength of .6943 microns.

Figure 16 gives the range correction at the most common SLR wavelength of .532 μ for a nominal atmosphere (P_H = 1000 mbar, T_H = 300°K, RH = 50%). The range correction is about 2.45 m at an elevation angle of 90° and increases to about 7 m at 20°. Generally, local safety regulations prohibit tracking below 20° at most SLR sites.

4.3 Residual Error Sources

Unlike more complicated atmospheric models which take into account local gradients in the meteorological parameters [Abshire and Gardner, 1985], the Marini-Murray and other spherical shell models [e.g. Herring, 1988] require only surface measurements of pressure, temperature, and relative humidity at the geodetic site. Such measurements are easy to obtain operationally and account for the popularity of the latter models among space geodesists. However, residual range errors following the application of these models are due to three sources: (1) errors in measurement of the surface meteorological parameters which are input to the model, (2) deviations of the actual vertical profiles (due to winds, complex temperature lapse rates, etc.) from that predicted theoretically by the assumption of hydrostatic equilibrium, and (3) the total failure of the spherical shell model to account for transverse gradient effects.

The magnitude of the first error source, sensor input errors, is relatively easy to analyze. Using the Marini-Murray (or other) model, one can compute the sensitivity to input errors for surface pressure, temperature, and humidity as in Figure 17. The figure shows that, at a worst case elevation angle of 20°, the model error is 8 mm for a 1 mbar pressure error. Repeated calibrations of onsite pressure sensors against NBS-traceable standards show routine agreement to 0.3 to 0.4 mbar suggesting that ground sensor errors contribute no more than about 3 mm at 20° elevation and only 1 mm at zenith. Measurement errors in temperature and relative humidity contribute at the submillimeter level for all elevation angles.

The magnitude of error sources 2 and 3, which depend on the adequacy of the model itself, are much more difficult to estimate although attempts have been made. Hauser [1989] has investigated the possible deviation of the atmosphere from hydrostatic equilibrium, especially near mountain sites, and concluded that the expected error is less than 1 cm most of the time, even for elevation angles as low as 20°. It has also been determined via ray tracing techniques that the transverse gradient terms typically contribute less than one centimeter of range error for elevation angles above 20° [Abshire and Gardner, 1985]. Nevertheless, a one centimeter systematic atmosphere- induced error is the dominant error source in modern day SLR measurements.

4.4 Two-Color Laser Ranging

By measuring the pulse times-of-flight at two colors and multiplying the results by the velocity of light in vacuum, c, we obtain a measure of the optical path lengths through the atmosphere at the two wavelengths. Thus, the atmospheric refraction correction is given by

$$AC = \gamma(L_1-L_2) = \frac{\gamma c}{2}(\tau_1-\tau_2) \qquad (4.4.1)$$

where L_1 and L_2 are the optical path lengths and τ_1 and τ_2 are the measured roundtrip times of flight at the two wavelengths respectively and

$$\gamma=\frac{n_{g1}-1}{n_{g2}-n_{g1}} \qquad (4.4.2)$$

where n_{g1} and n_{g2} are the group refractive indices at the two wavelengths. Unfortunately, the wavelength dependence due to

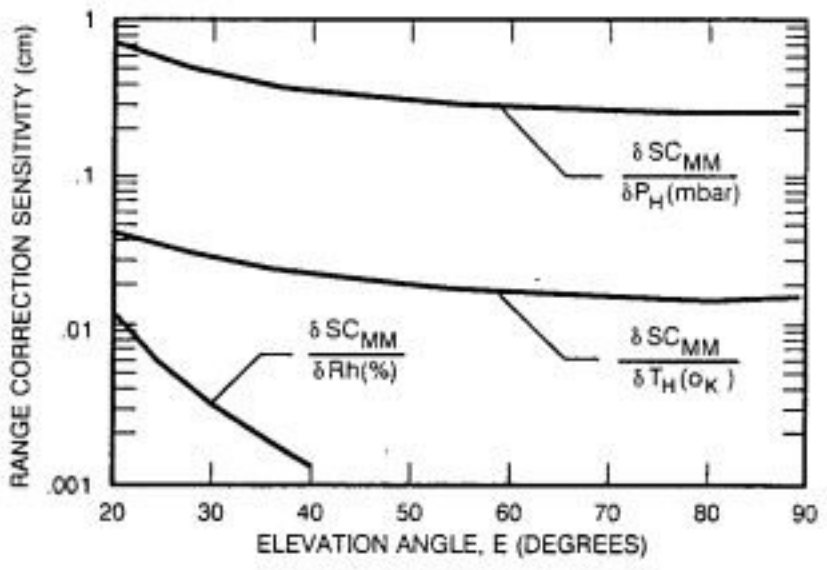

Fig 17. Sensitivity of the Marini-Murray range correction to measurement errors in surface pressure, temperature, and humidity.

Page17.jpg

the "dry" and "wet" components of the atmosphere are different [Owens, 1968]. Nevertheless, under normal conditions of modest humidity, γ can be well approximated by the expression [Abshire and Gardner, 1985]

$$\gamma = \frac{f(\lambda_1)}{f(\lambda_2) - f(\lambda_1)} \tag{4.4.3}$$

where $f(\lambda)$ is given by (4.2.2a). If we assume that the two times of flight are independently measured, we can express the expected variance in the atmospheric correction as

$$\sigma_{AC}^2 = (\gamma c/2)^2(\sigma_1^2 + \sigma_2^2) \tag{4.4.4}$$

where σ_1 and σ_2 are the RMS errors in the time of flight measurements at the wavelengths λ_1 and λ_2 respectively. In the ideal limit where the differential timing precision is determined only by the signal strength, one can write

$$\sigma_{AC} = \frac{\gamma c}{2}\left(\frac{\tau_{p_1}^2}{n_1} + \frac{\tau_{p_2}^2}{n_2}\right)^{1/2} \tag{4.4.5}$$

where τ_{p1} and τ_{p2} are the laser pulsewidths and n_1 and n_2 are the received photoelectron signal strengths at the two wavelengths respectively.

Figure 18 presents a simplified block diagram of a two color SLR system which is a slight modification of an earlier version [Degnan, 1985]. One modification is in the placement of the variable differential delay on the transmit side, as opposed to the receiver side, of the system. Since the second and third harmonic beams exiting from the nonlinear crystals which generate them are usually not collinear or parallel, they must be split off and made collinear prior to exiting the ranging system. Furthermore, for optimum performance, the beams should be independently magnified and collimated to achieve maximum illumination of the satellite target. Since the beams must be split and then recombined on the transmit side to satisfy the aforementioned requirements, it is a relatively simple matter (and much more efficient) to add a differential time delay at the same time. Furthermore, the stringent focusing requirements at the entrance slit of the streak tube receiver present another strong argument for locating the variable differential delay on the transmit side where the beams are well collimated.

A second innovation is the input of an optical pulse train to a third spatial channel of the streak tube receiver to monitor the sweep speed and linearity of the streak tube on a shot-by-shot basis for the ultimate timing accuracy and performance.

5. "Optimum" Wavelengths For Two Color SLR

In choosing "optimum" candidate wavelengths for successful two color ranging, there are a variety of technical issues the engineer must consider. These will be discussed in the ensuing subsections. As we shall now see, equation (4.4.5) for the RMS error in the atmospheric correction for the photon-limited case, combined with the radar link equation (3.1.1), points the way to the selection of an optimum wavelength. Since we want to minimize σ_{AC}, the inverse of (4.4.5) can serve as an overall system figure of merit. However, as we shall demonstrate in this section, these purely theoretical considerations must be tempered by several harsh realities, including constraints imposed by the available technology.

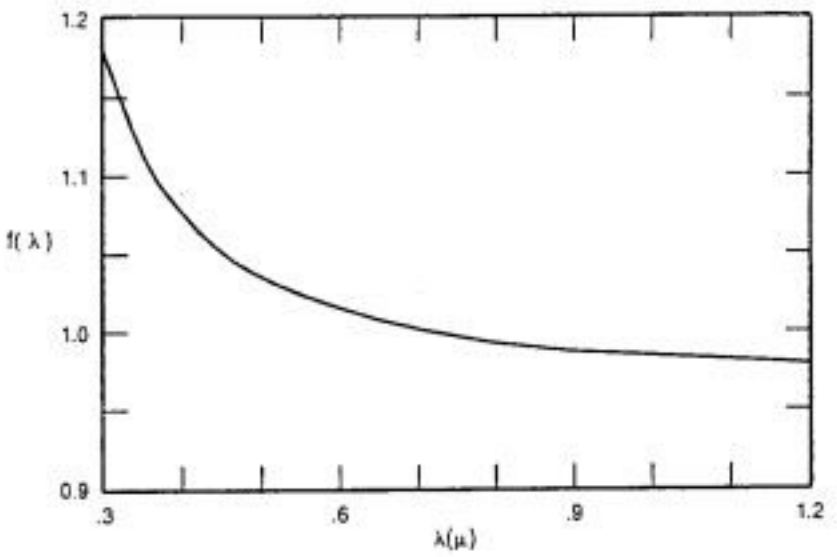

Fig. 19. Atmospheric dispersion in a standard atmosphere as a function of wavelength from the near ultraviolet to the near infrared.

5.1 Atmosphere

The dependence of (4.4.5) on the atmospheric dispersive function $f(\lambda)$ illustrates the need for adequate atmospheric dispersion between the two wavelengths in order to reduce the severity of the timing requirements. The atmospheric dispersion curve in Figure 19, which is a plot of (4.2.2a), strongly suggests that one wavelength be chosen to lie in the near ultraviolet. On the other hand, atmospheric attenuation in the spectral band between 0.3 and 0.7 microns, resulting from the combined effects of molecular (Rayleigh) and aerosol (Mie) scattering and ozone absorption, also increases rapidly in the near ultraviolet as shown in Figure 7. This will negatively impact the timing precision by lowering the system signal-to-noise (SNR) ratio at the UV wavelength. Furthermore, in choosing a laser wavelength, it is probably wise to avoid the strong water absorption lines in the spectral regions between 0.7 and 1.0 microns and beyond 1.1 micron. The high variability of water vapor total burden would impact both the day-to-day signal strength and cause the pulse group velocity to vary via the anomalous dispersion effect near an absorbing feature.

5.2 Laser Transmitter

The availability of lasers capable of generating high peak powers and ultrashort pulsewidths on the order of 35 picoseconds or less is also a consideration. Preference is generally given to solid state lasers because of the practical difficulties of using liquid dye lasers in the field. Over the past decade, much progress has been made in the development of highly tunable solid state lasers such as Alexandrite (700 to 810 nm) and Titanium-doped sapphire (600

Page18.jpg

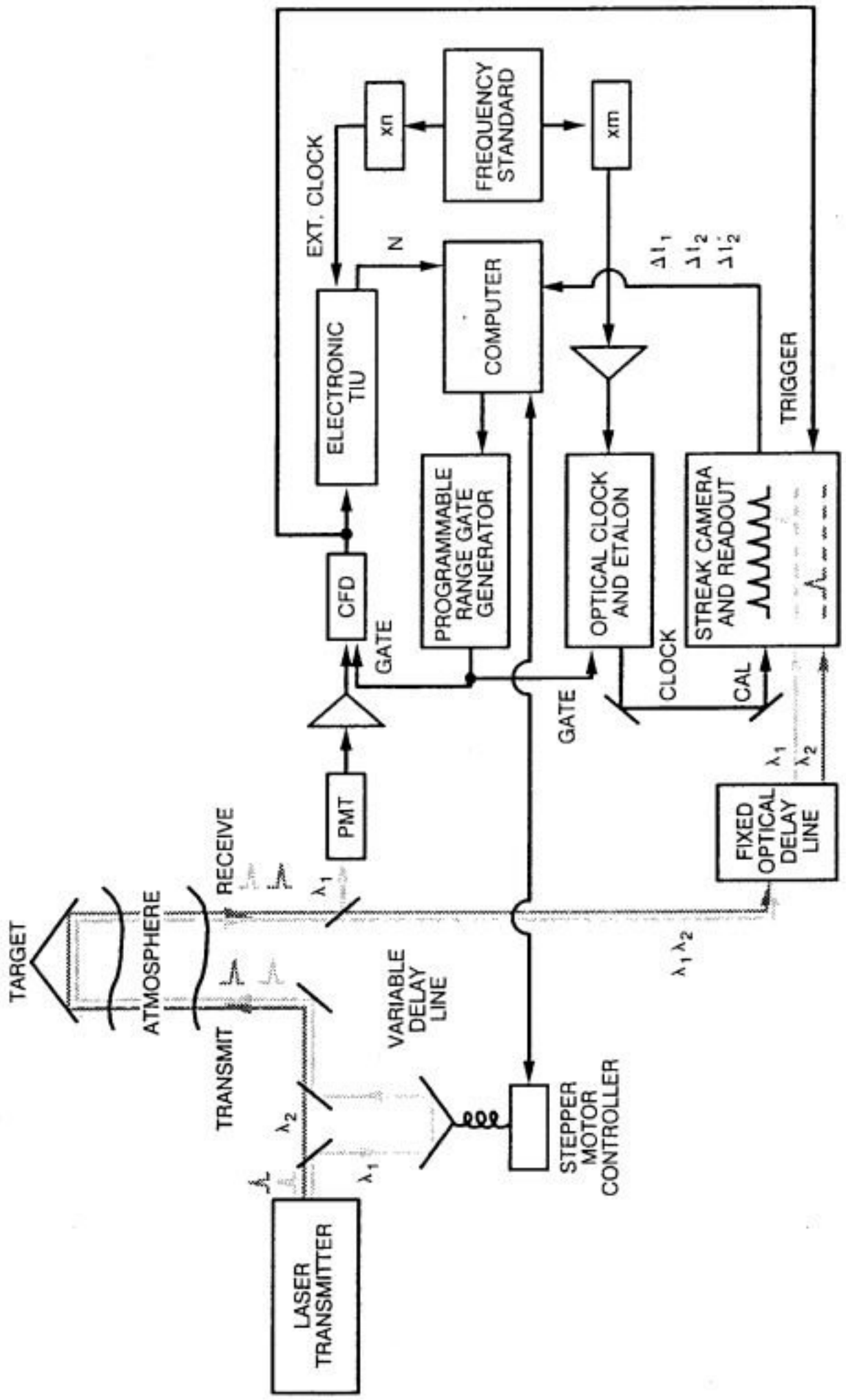

Fig. 18. Block diagram of a two color linear streak camera ranging system.

Page19.jpg

to 900 nm). The wide bandwidths of these new materials are capable of supporting subpicosecond pulsewidths whereas today's workhorse, Nd:YAG, is limited to about 10 picoseconds by its relatively narrow linewidth (120 GHz). However, high bandwidth comes at a price - i.e. lower gain - making the construction of high peak power Ti:Sapphire and Alexandrite devices more difficult.

Generally, the wavelengths in two color systems are generated from the fundamental wavelength λ_1 via nonlinear optical techniques such as harmonic generation in crystals or Raman shifting in gases. This assures simultaneity of emission and eliminates (thankfully) the need to synchronize the firings of two separate lasers with picosecond precisions. Reliance on nonlinear techniques, however, implies that the two wavelengths cannot be chosen independently of each other. In the case of harmonic generation, the second and third harmonic wavelengths are given by

$$\lambda_2=\frac{\lambda_1}{2} \qquad \lambda_3=\frac{\lambda_1}{3} \tag{5.2.1}$$

respectively.

In Raman shifting, a portion of the incident radiation at input frequency, ν_o is shifted by some fixed amount ν_s (the "Stokes shift") toward longer wavelengths relative to the fundamental. One also obtains frequencies at longer ("Stokes") and shorter ("Anti-Stokes") wavelengths, but these generally tend to be too weak to supply sufficient energy for satellite ranging. Large Stokes frequency shifts, and hence high dispersion between wavelengths, are obtained by Raman shifting in light gases. Hydrogen produces the largest shift of 4155 cm^{-1}, and photon conversion efficiencies as high as 80% have been reported. For example, one proposed two color SLR system uses the second harmonic of Nd:YAG (532 nm) in hydrogen to obtain a second wavelength output at 680 nm [Gaignebet et al., 1986].

A second consequence of harmonic or Raman generation is that the pulsewidth of the secondary wavelength is generally shorter than the pulsewidth of the fundamental. From the theory of harmonic generation [Degnan, 1979], the harmonic pulsewidths are approximately given by

$$\tau_2=\frac{\tau_1}{\sqrt{2}} \qquad \tau_3=\frac{\tau_1}{\sqrt{3}} \tag{5.2.2}$$

for low to moderate energy conversion efficiencies ($< 50\%$ - the usual case). Since, Raman generation depends on third order nonlinear processes, the pulsewidth dependence should be identical to that of third harmonic generation. At high conversion efficiencies, the harmonic pulsewidths tend to approach the fundamental pulsewidths.

5.3 Optical Detectors

Finally, the availability of high quantum efficiency optical detectors at the two laser wavelengths is important. If a common photocathode is to be used, such as in most streak camera schemes for performing differential timing, the photocathode must be sensitive at both wavelengths. However, since the images of the two return pulses can be spatially separated in the entrance slit of the streak camera, one can conceive of specially constructed streak tubes containing more than one photocathode material to obtain the highest sensitivity at both wavelengths. It may also be possible, at some future date, to do the necessary timing via electronic means, such as high speed GaAs technology, without resorting to streak camera technology although this capability has not yet been demonstrated.

Detector sensitivity at a particular wavelength is usually expressed as "spectral responsivity" in milliamperes/Watt. It is related to quantum efficiency by the equation

$$\eta_q(\lambda)=R(\lambda)\frac{hc}{\lambda e} \tag{5.3.1}$$

where $R(\lambda)$ is the detector spectral responsivity at wavelength λ, h is Planck's constant, and c is the velocity of light. Photoemissive detectors must be used in streak cameras. A composite responsivity curve, which is the envelope of individual responsivity curves for some common visible and near infrared photoemissive detectors [Slater, 1980; Zwicker, 1977] is illustrated in Figure 20.

A) "BEST" PHOTOEMISSIVE DETECTOR RESPONSIVITIES

WAVELENGTH (μ)	RESPONSIVITY	PHOTOCATHODE (+ WINDOW) MATERIAL
.3	50	S20
.35	60	K-Cs-Sb - (LIME GLASS)
.40	80	K-Cs-Sb - (LIME GLASS)
.45	70	K-Cs-Sb - (LIME GLASS)
.50	63	K-Cs-Sb - (LIME GLASS)
.55	64	GaAs (- 9741 GLASS)
.60	65	GaAs (- 9741 GLASS)
.65	67	GaAs (- 9741 GLASS)
.70	68	GaAs (- 9741 GLASS)
.75	69	GaAs (- 9741 GLASS)
.80	70	GaAs (- 9741 GLASS)
.85	68	GaAs (- 9741 GLASS)
.90	13	GaAs (- 9741 GLASS)
.98	9	GaInAs (+ 9741 GLASS)
1.02	.8	GaInAs (+ 9741 GLASS)
1.1	.2	S1

B) COMPOSITE GRAPH OF PHOTOEMISSIVE DETECTOR RESPONSIVITY

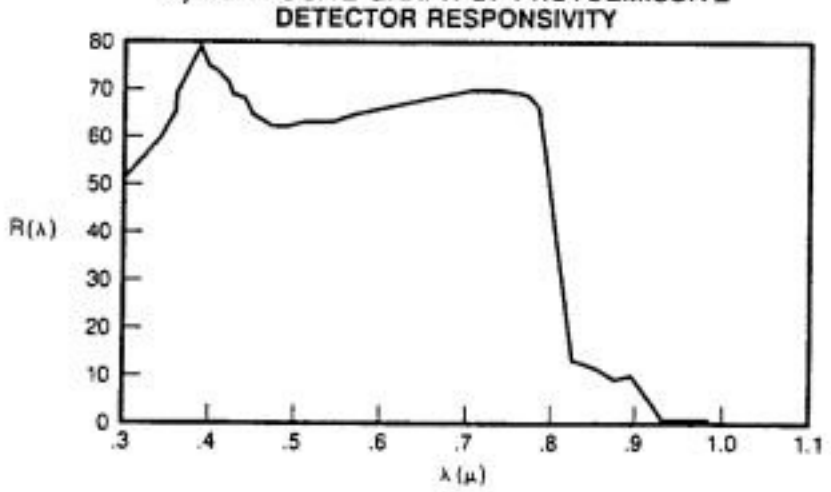

Fig. 20. Summary of "best" photoemissive detector responsivities from the near ultraviolet to the near infrared.

Page20.jpg

5.4 Wavelength Figure of Merit

In order to treat all potential system configurations on an equal basis, some assumptions are in order. We will assume that the fundamental laser, from which all other wavelengths are derived, is characterized by an energy E and a pulsewidth τ_p which is constant for all wavelengths. Thus, Equation (4.4.5) becomes

$$\sigma_{AC} = \gamma c \tau_p \sqrt{\frac{1}{\beta_1^2 n_1} + \frac{1}{\beta_2^2 n_2}} \qquad (5.4.1)$$

where β_1 and β_2 are pulsewidth scale factors which depend on the nonlinear process used to generate them as in (5.2.2). In addition, we recognize that wavelengths derived via nonlinear processes are obtained with some typical energy efficiency denoted by η_1 and η_2 respectively. For second and third harmonic generation in the ultrashort pulse regime, typical limiting efficiencies are $\eta_{sh} = .5$ and $\eta_{th} = .2$ respectively. If the fundamental wavelength is used as one of the two wavelengths, we will assign values of $\beta_f = 1$ and $\eta_f = 1$.

In order to derive a wavelength figure of merit, we must now bring together all of the wavelength dependent terms in equations (3.1.1) and (4.4.5). We obtain

$$F(\lambda_1,\lambda_2,E) = \frac{f(\lambda_1) - f(\lambda_2)}{f(\lambda_1)} \cdot \left[\frac{\lambda_1^4}{\eta_1\beta_1^2 R(\lambda_1) T_a^2(\lambda_1,E)} + \frac{\lambda_2^4}{\eta_2\beta_2^2 R(\lambda_2) T_a^2(\lambda_2,E)}\right]^{-1/2} \qquad (5.4.2)$$

where $f(\lambda)$ is the wavelength dispersion term in the Marini-Murray atmospheric correction formula, η_1 and η_2 and β_1 and β_2 are the energy conversion efficiencies and pulsewidth reduction factors respectively for the relevant nonlinear process, $R(\lambda)$ is the spectral responsivity, and $T_a(\lambda,E)$ is the one way atmospheric transmission function as a function of wavelength and elevation angle. The factor of λ^4 comes from the combined inverse square law dependence of the transmitter gain and target (retroreflector) gain on wavelength. The additional factor of λ associated with converting detector quantum efficiency to spectral responsivity cancels with a similar factor in (3.1.1) which converts transmitted energy to the number of transmitted photons. In plotting (5.4.2), we will use the envelope of the individual photoemitter responsivity curves in Figure 20 so that we present each wavelength in its most favorable light.

Figure 21 provides plots of the wavelength figure of merit as a function of the fundamental (laser) wavelength and elevation angle for the extremely clear atmosphere depicted in Figure 6. Parts (a), (b), and (c) correspond to elevation angles of 90, 45, and 20 degrees respectively. The three curves within each plot compare systems which use: (1) the fundamental and second harmonic wavelengths; (2) the fundamental and third harmonic wavelengths; and (3) the second and third harmonic wavelengths.

In spite of their greater dispersion, fundamental-third harmonic systems have the lowest figure of merit at all elevation angles due to a combination of poor detector performance at the fundamental and poor atmospheric transmission at the third harmonic. The performance of these systems peaks at a fundamental wavelength of about .97 microns independent of elevation angle.

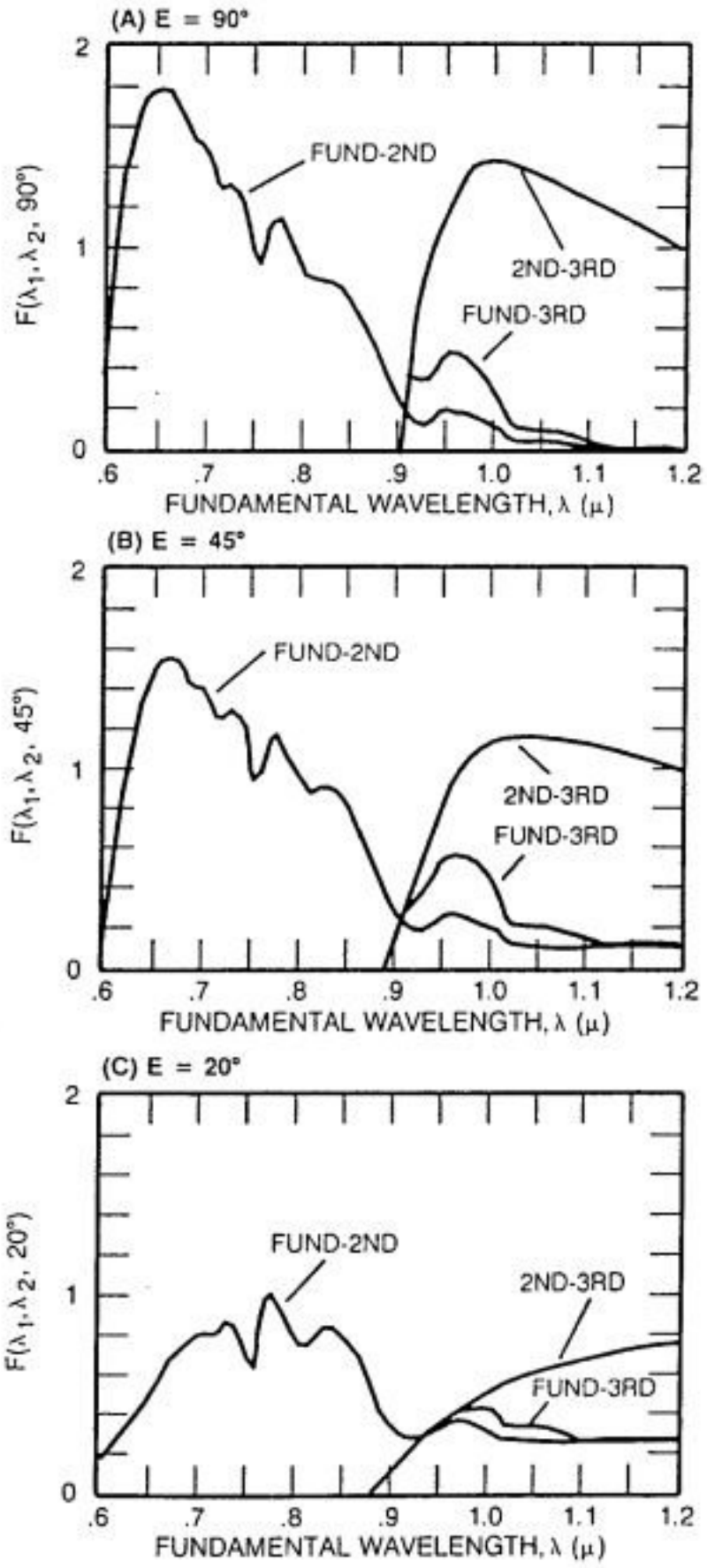

Fig. 21. Two color wavelength figure of merit for fundamental-second harmonic, fundamental-third harmonic, and second-third harmonic systems operating at elevation angles of (a) 90°, (b) 45° and (c) 20° respectively.

Page21.jpg

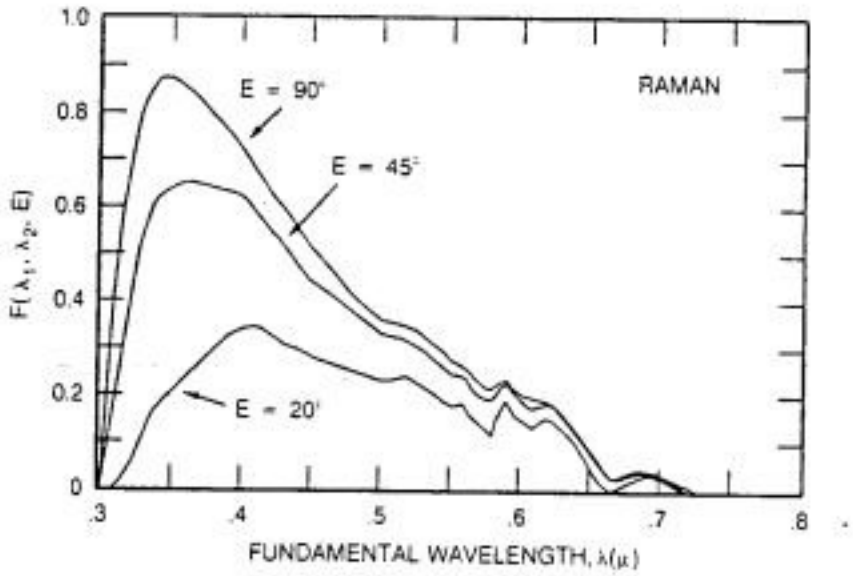

Fig. 22. Two color wavelength figure of merit for Raman systems operating at elevation angles of 90°, 45° and 20°.

At zenith, fundamental-second harmonic systems, operating at wavelengths of 670 and 335 nm, have the highest figure of merit (F = 1.75) but second-third harmonic systems, operating at wavelengths of 525 and 350 nm (fundamental = 1050 nm), are almost as good (F = 1.6). As one progresses to larger zenith angles, atmospheric attenuation in the ultraviolet begins to dominate and the optimum fundamental wavelength is shifted toward longer wavelengths with a corresponding reduction in wavelength figure of merit. Thus, the Nd:YAG laser, with a fundamental wavelength of 1064 nm and a very mature technology, is a near-optimum choice for a second-third harmonic system. However, a fundamental-second harmonic system which utilizes a Ti:Sapphire laser operating in the near infrared beyond 670 nm is a possible competitor.

Figure 22 suggests that a fundamental wavelength of about 400 nm is optimum for a hydrogen Raman-shifted laser and that these systems offer no real advantage over harmonic systems because of their lower wavelength figure of merit. This conclusion is further supported by the fact that there are no high power solid state lasers operating in the near ultraviolet. The principle short wavelength devices are excimer ("excited dimer") gas discharge lasers. At present, excimers cannot achieve ultrashort pulsewidths on the order of picoseconds, typically operate in the high atmospheric attenuation region of the spectrum below 360 nm, and are operationally less desirable than high power solid state lasers. Doubling or tripling solid state lasers to achieve a near ultraviolet wavelength prior to Raman shifting only decreases the overall wavelength figure of merit further by reducing the values for energy efficiency factors η_1 and η_2 in (5.4.2). However, this is somewhat offset by the reduction in pulsewidth (increased β values) resulting from nonlinear generation.

6. Satellite Effects

The analysis presented in Section 5 assumes that the laser pulsewidth is unmodified by the target satellite. This is not a valid assumption for most of the present constellation of target satellites - especially for the high altitude satellites, such as LAGEOS and ETALON, which are the primary targets for space geodesy applications. In this section, we provide a brief review of the basic properties of optical retroreflectors, discuss the arrays carried by present satellites, and investigate the feasibility of designing new geodetic satellites capable of supporting millimeter accuracy ranging systems.

6.1 Retroreflector Characteristics

For normally incident light, a single unspoiled retroreflector (cube corner) has a peak (on-axis) optical cross-section σ_{cc} defined by

$$\sigma_{cc}=\rho A_{cc}\left(\frac{4\pi}{\Omega}\right)=\rho A_{cc}\left(\frac{4\pi A_{cc}}{\lambda^2}\right) \qquad (6.1.1)$$

where ρ is the cube corner reflectivity, $A_{cc}=\pi R_{cc}^2$ is the light collecting area of the corner cube, and $4\pi/\Omega$ is the on-axis retroreflector gain where Ω is the effective solid angle occupied by the far field diffraction pattern (FFDP) of the retroreflector. For a circular entrance aperture, the FFDP of the reflected wave is the familiar Airy function given by [Born and Wolf, 1975]

$$\sigma(x)=\sigma_{cc}\left(\frac{2J_1(x)}{x}\right)^2 \qquad (6.1.2a)$$

where

$$x = kR_{cc}\sin(\theta) \qquad (6.1.2b)$$

and θ is the angle from the cube face normal. The Airy pattern consists of a main central lobe surrounded by weak rings. The angular half-width from the beam center to the first null is given by the first nonzero root of the Bessel function J_1 which, with (6.1.2b), yields the formula

$$\theta_{null}=1.22\frac{\lambda}{D_{cc}} \qquad (6.1.3)$$

where λ is the wavelength and $D_{cc} = 2\ R_{cc}$ is the diameter of the retroreflector.

At arbitrary incidence angle, the area in (6.1.1) is reduced by the factor [Minott, 1974]

$$\eta(\theta_{inc})=\frac{2}{\pi}(\sin^{-1}\mu-\sqrt{2}\,\mu\tan\theta_{ref})\cos\theta_{inc} \qquad (6.1.4)$$

where θ_{inc} is the incident angle and θ_{ref} is the internal refracted angle as determined by Snell's law, i.e.

$$\theta_{ref}=\sin^{-1}\left(\sin\frac{\theta_{inc}}{n}\right) \qquad (6.1.5)$$

Page22.jpg

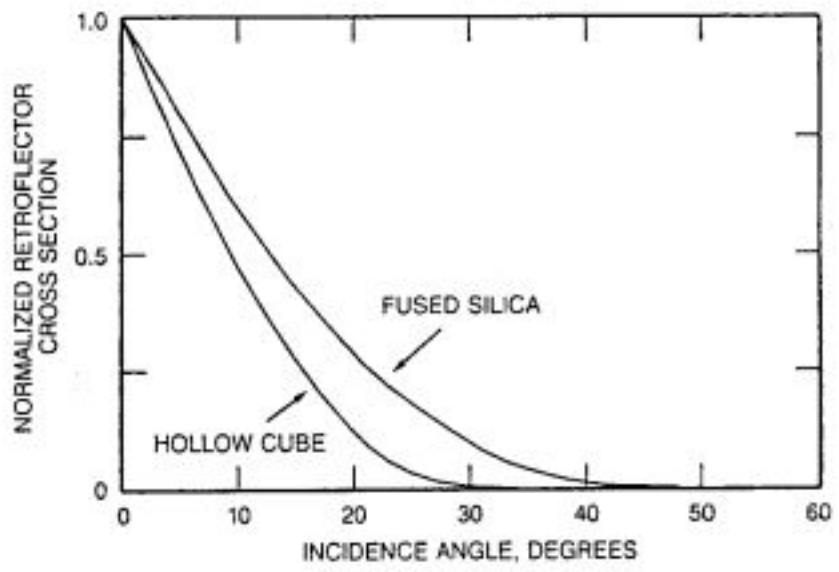

Fig. 23. Normalized cross-section as a function of incidence angle for hollow and fused silica retroreflectors.

where n is the cube index of refraction. The quantity μ is given by the formula

$$\mu = \sqrt{1 - 2\tan^2\theta_{ref}} \tag{6.1.6}$$

Thus the peak optical cross-section in the center of the reflected lobe falls off as

$$\sigma_{eff}(\theta_{inc}) = \eta^2(\theta_{inc})\sigma_{cc} \tag{6.1.7}$$

Figure 23 shows the falloff of optical cross-section with incidence angle for the two most common retroreflectors - hollow (n=1) and quartz (n=1.455). Note that, for a solid quartz cube, the optical cross-section falls to half its on-axis value at roughly 13° incidence angle and is effectively zero beyond about 40°. The cross-section for a hollow cube corner falls to half its normal incidence value at about 9° and is effectively zero beyond about 30°.

One can further limit the effective incidence angle over which the retroreflector responds by recessing the reflector in its holder. It can be easily shown that the effective area of the elliptical entrance aperture, as limited by the recess, is given by

$$A_{eff}(\theta_{inc}) = A_{cc}\left(1 - \frac{\tan\theta_{inc}}{\tan\theta_{max}}\right) \tag{6.1.8a}$$

where

$$\theta_{max} = \cot^{-1}\left(\frac{d}{D_{cc}}\right) \tag{6.1.8b}$$

and d is the depth of the recess.

6.2 Velocity Aberration

As mentioned previously, the far field diffraction pattern (FFDP) of a cube corner with a circular entrance pupil function corresponds to the familiar Airy pattern consisting of a single main lobe surrounded by low intensity rings. If there were no relative motion between the satellite and the target, the center of the FFDP would fall on the instantaneous line of sight between the target and satellite. However, due to the relative velocity between the satellite and the target, the coordinates of the FFDP are translated. The magnitude of the angular displacement in the FFDP is given by the equation [Minott, 1976]:

$$\alpha(h_s,\theta_{zen},\omega) = \alpha_{max}(h_s)\sqrt{\cos^2\omega + \Gamma^2(h_s,\theta_{zen})\sin^2\omega} \tag{6.2.1}$$

where the maximum value, α_{max}, is given by the expression

$$\alpha_{max}(h_s) = \frac{2}{c}\sqrt{\frac{R_E^2 g}{R_E + h_s}} \tag{6.2.2}$$

and

$$\Gamma(h_s,\theta_{zen}) = \sqrt{1 - \left(\frac{R_E \sin\theta_{zen}}{R_E + h_s}\right)^2} \tag{6.2.3}$$

and R_E is the Earth radius, g = 9.8 m/sec^2 is the gravitational acceleration at the surface, h_s is the satellite height above sea level, c is the velocity of light, and the angle ω is given by

$$\omega = \cos^{-1}[(\hat{r}x\hat{p})\cdot\hat{v}] \tag{6.2.4}$$

where $\hat{r}, \hat{p}$, *and* $\hat{v}$ are all unity length vectors in the directions of the satellite position vector (relative to the center of the Earth), the line-of-sight vector from station to satellite, and the satellite velocity vector respectively. Since $\Gamma(h_s, \theta_{zen})$ is always less than unity, equation (6.2.1) has an effective "minimum" value, for a given θ_{zen}, when $\omega = \pi/2$. Thus,

$$\alpha_{min}(h_s,\theta_{zen}) = \alpha_{max}(h_s)\Gamma(h_s,\theta_{zen}) \tag{6.2.5}$$

The maximum and minimum angular displacements of the FFDP are plotted as a function of satellite height in Figure 24 assuming a maximum θ_{zen} of 70°. It should be noted from the figure that the maximum angular displacement decreases with altitude and that the maximum and minimum values converge for high satellites. At ETALON altitudes (19,000 Km), for example, the angular displacement is roughly constant at about 26 μrad.

If the target FFDP is angularly narrow relative to the size of the velocity aberration displacement, the receiver will lie on the low signal edge of the FFDP or lie outside the FFDP entirely. For example, consider a moving retroreflector whose face is normal to the ranging system line-of-sight. The cross-section is given by

Page23.jpg

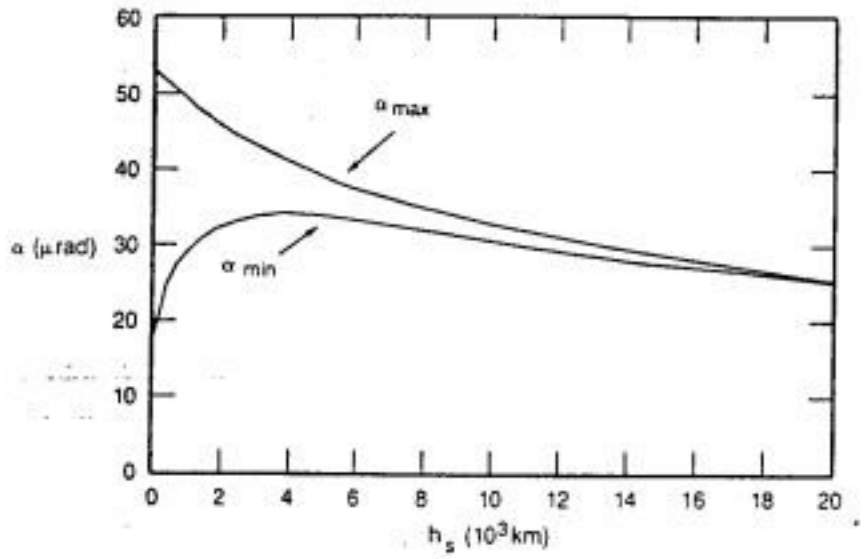

Fig. 24. Maximum and minimum far field diffraction displacement angle induced by velocity aberration as a function of satellite altitude assuming a minimum tracking elevation angle of 20°.

(6.2.1a) with $x = kR_{cc}\sin(\alpha) - kR_{cc}\alpha$ where alpha is the instantaneous angular displacement caused by velocity aberration. If $\alpha \ll \alpha_{null}$, the reduction in cross-section is negligible. However, if α is large, the reflected beam will "miss" the receiver and low or nonexistent signal levels will result. For non-normal incidence angles, the reflected FFDP is no longer circularly symmetric since the collecting (and transmitting) aperture of the retroreflector appears as an ellipse to the range receiver. The FFDP peak is again along the instantaneous receiver line-of-sight, but the FFDP is now given by the two-dimensional Fourier transform of the elliptic entrance aperture of the corner cube. The velocity aberration causes the retroreflector response to be reduced relative to the peak value given by (6.1.7). This reduction is greater for velocity vectors which are parallel to the long axis of the ellipse because of the faster falloff of the FFDP with angle in this direction.

6.3 Retroreflector "Spoiling"

To partially recover the target gain lost due to velocity aberration in large retroreflectors, the retroreflector is often "spoiled". The goal of "spoiling" is to concentrate more reflected energy into the annular region bordered by α_{max} and α_{min}. Ideally, one would like to uniformly spread the energy within the annular ring yielding an optimum cross-section given by

$$\sigma_{ideal} = \rho A_{cc}\left(\frac{4\pi}{\Omega_{cc}}\right) = \rho A_{cc}\left(\frac{4}{\alpha_{max}^2 - \alpha_{min}^2}\right) \qquad (6.3.1)$$

where the quantity in parentheses is the ideal effective target gain and Ω_{cc} is the solid angle subtended by the annular ring of interest. However, conventional spoiling techniques generally result in average optical cross-sections which agree only within an order of magnitude of the ideal limit described by (6.3.1).

Spoiling is usually accomplished by introducing slight variations into the cube corner dihedral angles (typically less than two arcseconds). This creates a complicated FFDP which, for an incident beam normal to the cube face, breaks the initial single main Airy lobe into 2N lobes (where N = 1 to 3 is the number of spoiled dihedral angles) distributed within an angular annulus. The mean angular radius of the annulus increases linearly with the dihedral offset angle from a perfect cube and, from diffraction theory (see 6.1.3), one expects the effective angular width of the various lobes to depend inversely on cube diameter.

Each of the 2N lobes originates from a different sector of the retroreflector entrance aperture. In fact, the FFDP of each lobe is determined by the two-dimensional Fourier transform of the projection of a 180°/2N sector of the circular (assumed) retroreflector entrance aperture into a plane perpendicular to the line-of-sight between the satellite and the station. The distribution of energy within this "annulus" is therefore highly nonuniform. Furthermore, the effective area for each lobe is reduced to

$$A_{eff} = \eta(\theta_{inc})\frac{A_{cc}}{2N} \qquad (6.3.2)$$

Substituting the latter expression into (6.1.1), we obtain an approximate expression for the peak optical cross-section at the center of one of the 2N lobes for the spoiled retroreflector at arbitrary incidence angle

$$\sigma_{peak}(\theta_{inc}, N) = \eta^2(\theta_{inc})\frac{\sigma_{cc}}{(2N)^2} \qquad (6.3.3)$$

One can also "spoil" the retroreflector by placing or grinding a weak lens onto the entrance face. This approach retains the single central lobe of the unspoiled cube corner while reducing its peak amplitude and spreading the energy over a wider solid angle, Ω. This approach yields a peak cross-section given by

$$\sigma_{lens} = \rho A_{cc}\left(\frac{4\pi}{\Omega}\right) \qquad (6.3.4)$$

and can be effective when velocity aberrations are sufficiently small.

6.4 Satellite Optical Cross-Section

As noted previously, the optical cross-section which can be achieved with a single retroreflector is limited by the need to compensate for velocity abberation effects. Received SLR signals can only be enhanced by summing the contributions of several retroreflectors. Modern geodetic target satellites (e.g., STARLETTE, LAGEOS, and ETALON) are all designed to be spherical in shape in order to avoid the large pulse spreading caused by earlier flat panel arrays when viewed at non-normal incidence. The spherical shape also simplifies the modelling of nonconservative forces acting on the satellite.

Satellite array size is largely determined by the satellite altitude since more retroreflectors are required to achieve reasonable signal-to-noise ratios over longer slant ranges. Thus,

Page24.jpg

STARLETTE (960 Km), LAGEOS (5900 Km), and ETALON (19,200 Km) have diameters of 12, 60, and 129.4 cm and average optical cross-sections of .65, 7, and 60 million square meters respectively.

Let us consider a spherical satellite which is uniformly covered with retroreflectors. The density of cube corners, as a function of incidence angle, is easily seen to be

$$N(\theta_{inc})d\theta_{inc}=\frac{N}{2}\sin\theta_{inc}d\theta_{inc} \tag{6.4.1}$$

where N is the total number of reflectors on the satellite. To obtain a simple expression for the overall target cross-section, we approximate the sum over all of the retroreflectors within the allowed range of incidence angle by the following integral

$$\sigma=\sigma_{cc}\int_0^{\frac{\pi}{2}}d\theta_{inc}N(\theta_{inc})\eta^2(\theta_{inc}) \tag{6.4.2}$$

where we have used (6.1.7). If the retroreflectors are not recessed in their holders, $\eta(\theta_{inc})$ is given by (6.1.4). If their angular response is limited by the recess, (6.1.8a) suggests that the variation can be well-approximated by the expression

$$\eta(\theta_{inc})=1-\frac{\theta_{inc}}{\theta_{max}} \tag{6.4.3}$$

where θ_{max} is given by (6.1.8b). Actually, (6.4.3) is an excellent approximation to (6.1.4) as well provided we choose θ_{max} equal to .54 rad (31°) for hollow cubes or .75 rad (43°) for solid cubes respectively (see Figure 20). Substituting (6.4.1) and (6.4.3) into (6.4.2) and evaluating the resulting integrals yields a simple expression for the target cross-section

$$\sigma=\frac{\sigma_{cc}N}{2}\left[1-\frac{\sin^2\left(\frac{\theta_{max}}{2}\right)}{\left(\frac{\theta_{max}}{2}\right)^2}\right] \tag{6.4.4}$$

Let us now examine the validity of (6.4.4) by substituting LAGEOS values. The LAGEOS satellite has a radius R = 29.8 cm and is imbedded with 426 retroreflectors (422 fused quartz and 4 germanium) each having a clear aperture diameter D_{cc} of 3.81 cm. Ignoring the fact that four cubes are germanium, we choose N = 426 and a value of θ_{max} = .75 rad for solid quartz cubes. We now use a value σ_{cc} = 2.834 x 10^6 in agreement with the input values to the RETRO computer program as determined during LAGEOS testing and evaluation [Fitzmaurice et al., 1977]. Substituting the latter values into (6.4.4) yields

$$\sigma_{LAGEOS}=9.8\sigma_{cc}=2.78\times10^7 m^2 \tag{6.4.5}$$

This is roughly equal to the peak value computed by the much more detailed RETRO program which showed a range of values between .54 and 2.7 x 10^7 m^2. Equation (6.4.4) tends to overestimate the actual cross-section because it assumes a peak cross-section reduced by geometric, but not velocity aberration, effects. Equation (6.4.5) implies that the LAGEOS array cross-section is roughly 9.8 times that of a single cube corner at normal incidence.

6.5 Satellite Impulse Response and Target Speckle

An individual retroreflector responds as a point source and hence does not spread the laser pulse in time. However, with a typical array of retroreflectors, the laser pulse arrives at the "reflection center" of each retroreflector at a slightly different time leading to a broadening of the received pulse [Degnan, 1985]. The location of the "reflection center" for an individual solid cube corner reflector is given by [Fitzmaurice et al., 1977; Arnold, 1978]

$$\Delta R(\theta_{inc})=nL\sqrt{1-\left(\frac{\sin\theta_{inc}}{n}\right)^2}=nL\cos\theta_{ref} \tag{6.5.1}$$

where $\Delta R(\theta_{inc})$ is measured from the center of the front face of the cube corner to the reflection point, L is the vertex to front face dimension, n is the refractive index of the corner cube material, θ_{inc} is the angle of incidence, and θ_{ref} is the corresponding refraction angle. From Figure 25, it can be seen that a cube at an

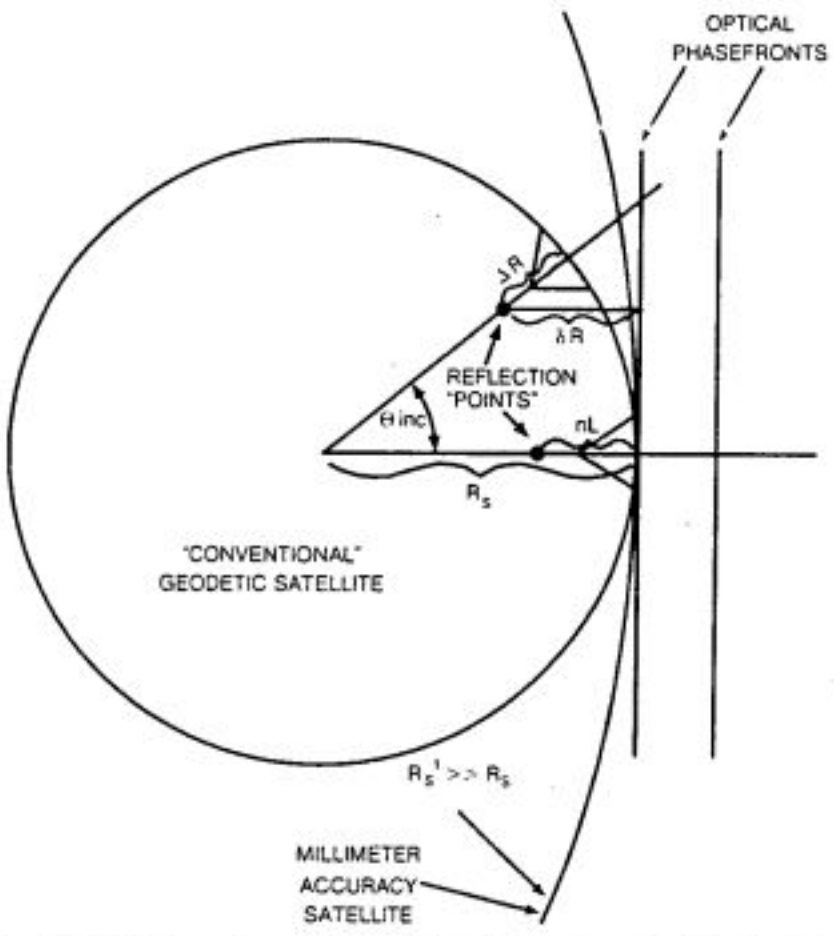

Fig. 25. Definitions of quantities used in the discussion of satellite impulse response. Satellites capable of supporting millimeter accuracy two color measurements are characterized by larger radii, high retroreflector densities, and limited angular field of view. The large satellite radius provides a better "match" to the incoming planar phasefront.

Page25.jpg

angle θ_{inc} to the incident wave produces a time delay, relative to the surface of the satellite closest to the ranging station ($\theta_{inc} = 0$), given by

$$\Delta t(\theta_{inc}) = \frac{2}{c}\{R_s - [R_s - \Delta R(\theta_{inc})]\cos\theta_{inc}\}$$
$$= \frac{2R_s}{c}\left\{1 - \cos\theta_{inc}\left[1 - \frac{nL}{R_s}\cos\theta_{ref}\right]\right\} \quad (6.5.2)$$

where R_s is the satellite radius. It should also be noted that the differential delay between target reflection points also introduces a random phase delay between individual reflectors. Thus, if the temporal profiles from multiple cubes overlap at the range receiver, the electric fields will interfere with each other in a random way from shot to shot resulting in target "speckle". On average, however, the return waveform from the satellite should behave as if each of the retroreflectors is an incoherent source. This was an implicit assumption in our derivation of target optical cross-section in Section 6.4.

In the same spirit, the "average" satellite temporal response can then be estimated by summing the weighted (incoherent) returns from each of the retroreflectors. Using the simple model for a spherical satellite introduced in section 6.5, the impulse response can be approximated by

$$I(t) = \sigma_{cc}\frac{N}{2}\int_0^{\frac{\pi}{2}} d\theta_{inc}\sin\theta_{inc}\,\eta^2(\theta_{inc})\,\delta[t - \Delta t(\theta_{inc})] \quad (6.5.3)$$

where the geometric weighting factor is given by (6.1.4) or (6.4.3), $\Delta t(\theta_{inc})$ is given by (6.5.2), and the delta function $\delta[t - \Delta t(\theta_{inc})]$ represents an infinitely short laser pulse waveform incident on the satellite. From (6.5.2), we see that the delta function is nonzero only when the condition

$$\cos\theta(\tau,e,n) = \frac{1-\tau}{1 - e\sqrt{1 - \frac{1}{n^2} + \left[\frac{\cos\theta\,\tau,e,n)}{n}\right]^2}} \quad (6.5.4)$$

holds where we have defined the new variables

$$\tau = \frac{ct}{2R_s} \qquad e < \tau < \tau_{max}$$

$$e = \frac{nL}{R_s} \qquad \tau_{max} = 1 - \cos\theta_{max}\left\{1 - e\sqrt{1 - \frac{1}{n^2} + \left(\frac{\cos\theta_{max}}{n}\right)^2}\right\} \quad (6.5.5)$$

The variable τ is a normalized time, expressed in units of the roundtrip transit time of light from the surface of the satellite to the center and back, and ϵ is the ratio of the optical depth of an individual cube to the satellite radius. The minimum and maximum values of τ are determined by setting θ_{inc} equal to zero and θ_{max} respectively in (6.5.4) and solving for t. The total pulse duration, measured at the baseline, is given by $\Delta t = (2R_s/c)(\tau_{max} - \epsilon)$.

From (6.5.3) and (6.5.4), the satellite impulse response can now be expressed as a function of the variables τ, ϵ, n and θ_{max}, i.e.

$$I(\tau,e,n,\theta_{max}) = \sigma_{cc}\frac{N}{2}\sin\theta(\tau,e,n)\left[1 - \frac{\theta(\tau,e,n)}{\theta_{max}}\right]^2 \quad (6.5.6)$$

where $\theta(\tau,\epsilon,n)$ is defined by (6.5.4). In the limit of large satellites ($\epsilon \to 0$), (6.5.4) reduces to the simple form

$$\theta(\tau,0,n) = \cos^{-1}(1-\tau) \quad (6.5.7)$$

and (6.5.6) becomes

$$I(\tau,0,n,\theta_{max}) = \sigma_{cc}N\tau\left(1 - \frac{\tau}{2}\right)\left[1 - \frac{\cos^{-1}(1-\tau)}{\theta_{max}}\right]^2 \quad (6.5.8)$$

The quantity ϵ is typically small and, for nonzero values of ϵ, (6.5.4) can be easily solved by iteration using (6.5.7) as a starting point, i.e.

$$[\cos\theta(\tau,e,n)]_{j+1} = \frac{1-\tau}{1 - e\sqrt{1 - \frac{1}{n^2} + \left[\frac{[\cos\theta(\tau,e,n)]_j}{n}\right]^2}} \quad (6.5.9)$$

until it converges.

As an illustration, let us now use (6.5.6) to estimate the impulse response of the LAGEOS satellite. Substituting n = 1.455 (fused silica), L = 1.905 cm, and R_s = 29.8 cm into (6.5.5b), we obtain a value ϵ = .093. We recall that, for solid cube corners, we can use a value θ_{max} = 0.75 rad. Now, using (6.5.6) and (6.5.9), we obtain the plot of the LAGEOS impulse response shown in Figure 26. The profile shows the characteristic fast rise and long tail of the LAGEOS response. Furthermore, if we compute a

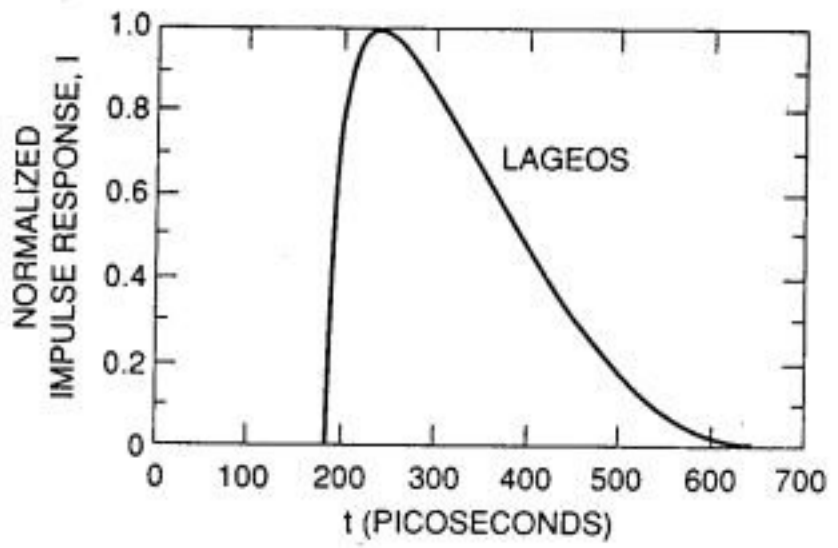

Fig. 26. Impulse response of the LAGEOS satellite as computed by our simple analytical model.

Page26.jpg

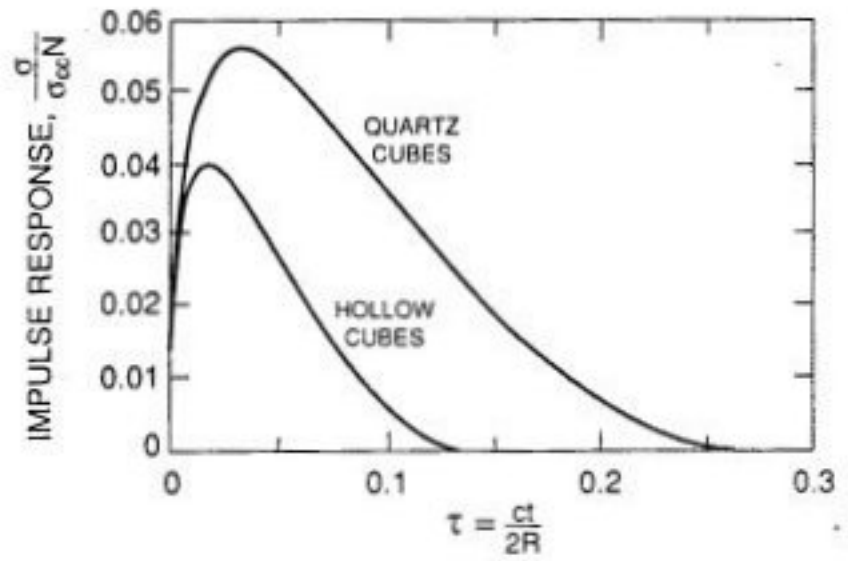

Fig. 27. Impulse response in the large satellite limit ($R_s \gg nL$) for both hollow and solid quartz cube corners.

center-of-mass correction from the centroid of this impulse response profile, we obtain a value of 250.2 mm which is in excellent agreement with the accepted value of 249 ± 1.7 mm [Fitzmaurice et al., 1977].

The impulse response in the large satellite limit, given by (6.5.8), is shown in Figure 27 for the case of solid quartz and hollow cubes. Note that the smaller field-of-view of the hollow cube results in both a narrower temporal width of the reflected pulse and a smaller target optical cross-section when compared to solid cubes.

6.6 *Feasibility of Millimeter Accuracy Satellites*

The principal technical challenge in designing a millimeter accuracy satellite to support two color observations at high altitudes is to provide high optical cross-section simultaneously with minimal pulse spreading. To achieve this with a spherical satellite, we must increase the satellite diameter and/or retroreflector density and simultaneously restrict the response to retroreflectors within a relatively small solid angle on the satellite surface about the station line of sight. Increasing the diameter provides; (1) a larger surface area for additional cube mounting which leads to higher cross-sections; and (2) makes the satellite surface a better match for the incoming planar phasefront of the laser beam as in Figure 25. Restricting the retroreflector field of view limits the target response to the fraction of the satellite surface which nearly matches the phasefront thereby controlling the amount of pulse spreading. In this subsection, we will attempt to quantify these rather qualitative statements.

The total time duration of the reflected pulse (0% to 0% intensity points) can be determined from (6.5.5), i.e.

$$\Delta t = \frac{2R_s}{c}(\tau_{max} - \epsilon)$$
$$= \frac{2R_s}{c}\left\{2\sin^2\left(\frac{\theta_{max}}{2}\right) + \epsilon\left[\cos\theta_{max}\sqrt{1 - \frac{\sin^2\theta_{max}}{n^2}} - 1\right]\right\} \quad (6.6.1)$$

which, in the limit of small maximum incidence angles, reduces to

$$\Delta\tau \sim \frac{R_s}{c}\theta_{max}^2\left[1 - \epsilon\left(1 + \frac{1}{n^2}\right)\right] \quad (6.6.2)$$

In the same limit, Eq. (6.4.4) for the satellite optical cross-section reduces to

$$\sigma \sim \frac{\sigma_{cc}N}{24}\theta_{max}^2 \quad (6.6.3)$$

As mentioned earlier, the angular response can be restricted by recessing the retroreflectors in their holders. Solving for θ_{max} in (6.6.2) and substituting the result into (6.6.3) yields

$$\sigma = \frac{\sigma_{cc}N}{24}\frac{c\Delta t_{max}}{R_s\left[1 - \frac{nL}{R_s}\left(1 + \frac{1}{n^2}\right)\right]} \quad (6.6.4)$$

We can now express the total number of retroreflectors as

$$N = \beta\frac{4\pi R_s^2}{A_{cc}} \quad (6.6.5)$$

where β is a "packing density" (= .435 for LAGEOS) which represents the fraction of total surface area occupied by the cube faces. Substituting (6.6.5) into (6.6.4) and using (6.1.1) yields our final result

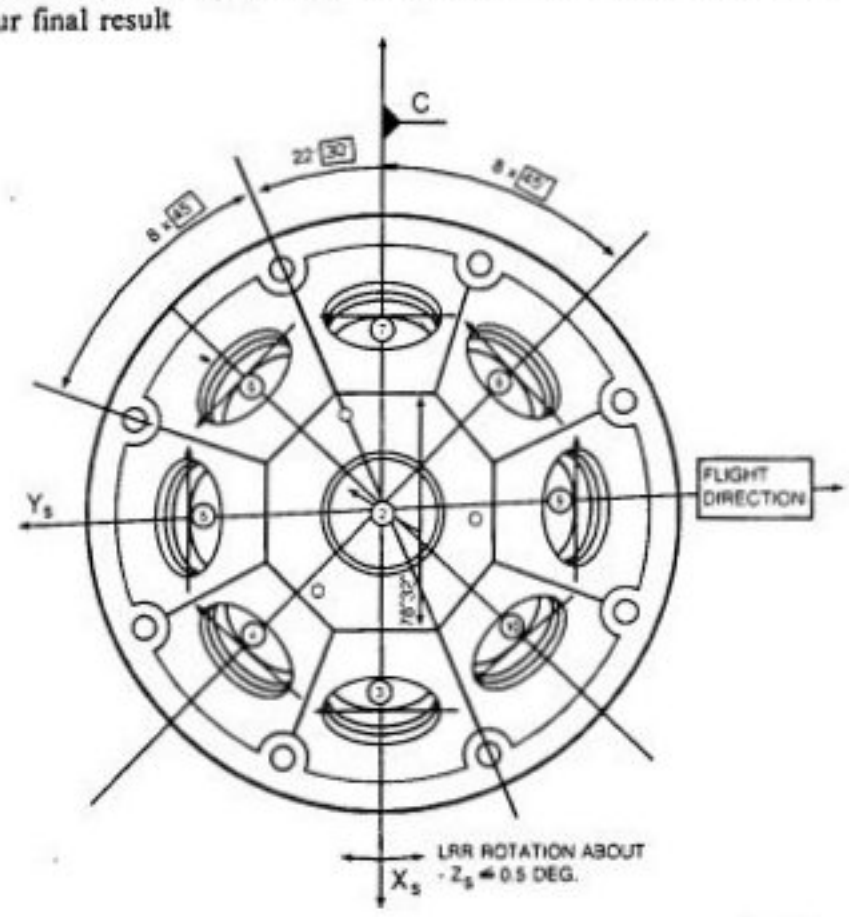

Fig. 28. ERS-1 target array consisting of one nadir-viewing cube and eight additional cubes arranged in a ring.

Page27.jpg

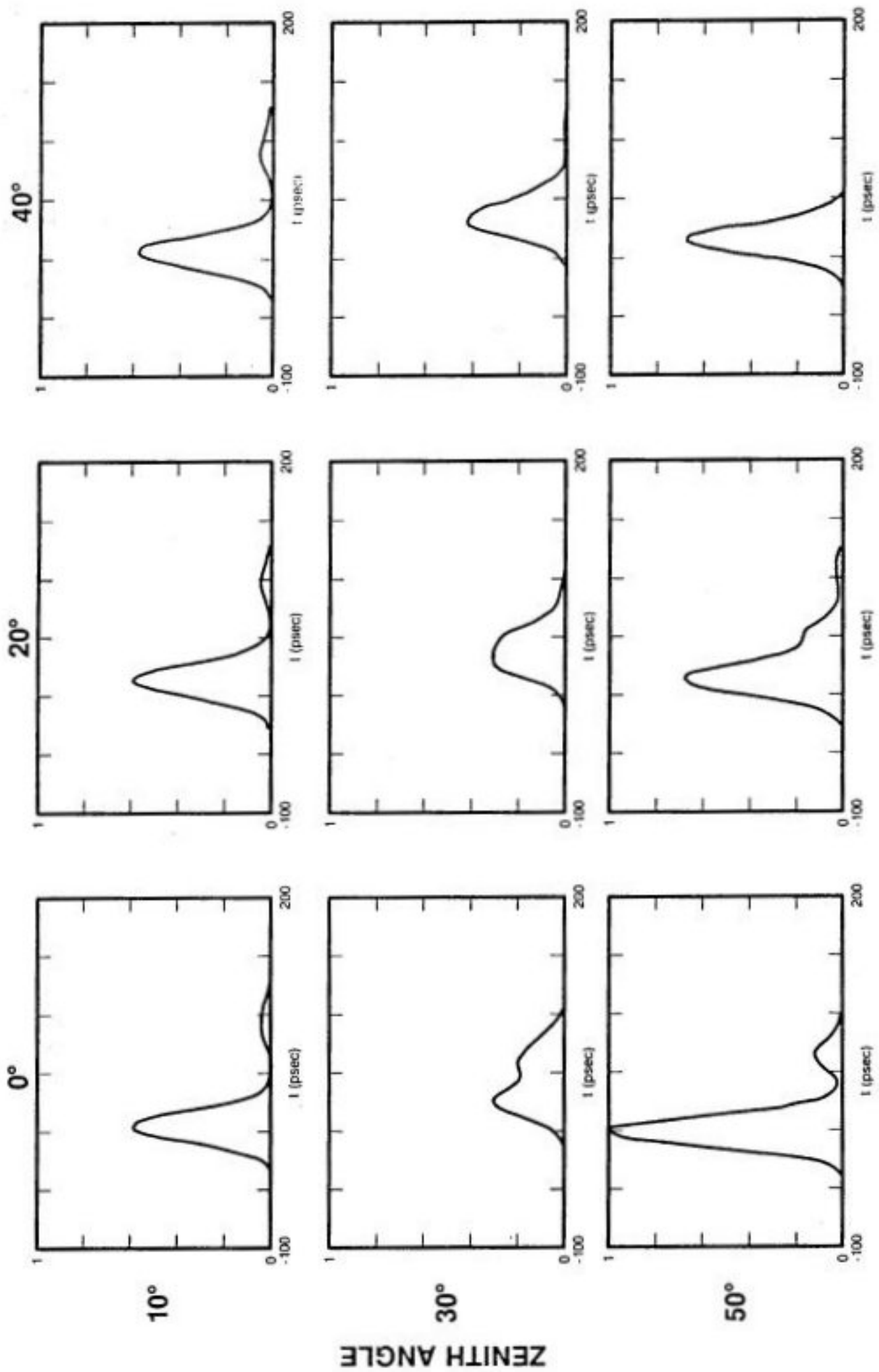

Fig. 29. Predicted temporal waveforms from the ERS-1 satellite as a function of "zenith" and "azimuth" angle for a 50 picosecond laser pulse incident on the satellite. "Zenith" angle is defined here as the angle between the incident laser beam and the normal to the nadir-viewing cube face. For an "azimuth" angle of zero degrees, the projection of the beam center into the plane of Figure 28 intersects the center of one of the eight ring cubes.

Page28.jpg

$$\sigma \sim \frac{2\pi^2 \rho}{3\Omega} \frac{\beta R_s c \Delta t}{\left[1 - \frac{nL}{R_s}\left(1 + \frac{1}{n^2}\right)\right]} \qquad (6.6.6)$$

The product $\beta R_s c\Delta t$ in (6.6.6) quantifies our earlier statement that we must increase the retroreflector packing density, β, and/or the satellite radius, R_s, to retain a high cross-section while simultaneously restricting the retroreflector angular field-of-view to reduce the amount of pulse-broadening. Equation (6.6.6) also suggests that cube corner diameter does not play a major role except to the extent that it can be adjusted to optimally fill the desired annular solid angle represented by Ω. Of course, since satellite accelerations due to atmospheric drag are proportional to the ratio of cross-sectional area to mass, the satellite mass must also be increased proportionately to achieve the same insensitivity to drag effects.

For near term experiments, the small size of STARLETTE makes it an attractive target for testing and evaluating two color systems or for testing atmospheric models. Furthermore, its low altitude (960 Km) and moderate target cross section results in relatively high received signal levels. AJISAI, also in a relatively low 1375 Km orbit, consists of small clusters of retroreflectors separated by large reflecting panels and provides high signal strength. Unfortunately, the satellite is quite large and simultaneous returns from several retro clusters results in a complicated satellite signature [Sasaki and Hashimoto, 1987; Prochazka et al., 1991]. LAGEOS spreading is in excess of 150 picoseconds [Fitzmaurice et al., 1977] although, with sufficiently short laser pulses (<50 psec), individual retro rings should be resolvable at certain satellite orientations. (Note that the simple satellite model presented here gives an average response over the full range of satellite orientations and shows none of the structure expected for a particular orientation.) The LAGEOS pulse spreading combined with relatively low signal returns, measured at the few to several tens of photoelectron level for most systems, would make the necessary differential timing very difficult [see (4.4.5)].

Another useful target for two-color system evaluation is the recently launched European Earth Remote Sensing satellite, ERS-1. It flies at a relatively low altitude (<800 Km) and has a small compact target consisting of one nadir-viewing retroreflector surrounded by a uniformly spaced ring of eight identical cube corners at a nadir angle of 50° as in Figure 28. Approximate modelling of this satellite by the author indicates that sharp returns consisting of one or two peaks (well separated) can be obtained from most viewing angles as illustrated in Figure 29. At nadir angles between 0° and 15°, the nadir viewing cube is dominant whereas, for nadir angles between 30° and 70°, the ring provides a sharp return at virtually all azimuthal angles. At nadir angles between about 15° and 30°, there is some overlapping of returns and pulse distortion.

7. Summary

The size and precision of the international satellite laser ranging network has improved dramatically over the last seven years and has begun to attract new users within the scientific community. Today, SLR supports the study of plate tectonics and regional crustal deformation, Earth orientation and spin rate, gravitational fields, international time transfer, oceanography, topography, relativity, lunar physics, and fundamental physics. Subcentimeter range precisions are rapidly proliferating within the international network, and new satellites are being launched yearly. Present efforts to provide more uniform precision and truly global coverage should be continued.

Two color satellite laser ranging offers the potential of an order of magnitude improvement in ranging absolute accuracy, but the technique requires high precision differential time measurements. This is most easily accomplished with short pulses, high signal levels, and temporal averaging. The present paper performed engineering tradeoffs in an effort to identify those wavelengths and supporting hardware components which resulted in maximum signal strength. Various mathematical models of the ranging system and atmosphere were invoked to support the latter analysis. Existing satellites such as STARLETTE and ERS-1 should be suitable for testing and evaluating two color systems. However, to realize the full potential of two color techniques for space geodesy, it will be necessary to carry out these measurements to satellites at LAGEOS altitudes or higher. Unfortunately, existing high altitude satellites such as LAGEOS and ETALON have very marginal optical cross-sections and substantially broaden the return pulse. Larger diameter satellites, however, can be developed to improve two color performance.

In the application of laser range measurements to the computation of relative geodetic site positions or baselines, errors associated with the satellite force model in the "dynamic" method of analysis appear, to this author at least, to be a limiting error source and alternative methods of analysis should be investigated. Quasi-simultaneous geometric solutions, while not a viable option in earlier years, are more feasible today as a result of a denser and more reliable SLR network and the extended site visibility of high altitude satellites such as LAGEOS and ETALON [Degnan et al., 1991].

8. References

Abshire, J. B., and C. S. Gardner, Atmospheric refractivity corrections in satellite laser ranging, *IEEE Trans. on Geoscience and Remote Sensing*, GE-23, pp. 414-425, 1985.

Arnold, D. A., Optical and infrared transfer function of the LAGEOS retroreflector array, Final Report NASA Grant NGR 09-015-002, Smithsonian Institution Astrophysical Observatory, May 1978.

Born, M., and E. Wolf, *Principles of Optics*, Chapter 8, Pergamon Press, New York, 1975.

Cohen, S. C., J. J. Degnan, J. L. Bufton, J. B. Garvin, and J. B. Abshire, The Geoscience Laser Altimetry/Ranging System, *IEEE Trans. Geoscience and Remote Sensing*, GE-25, pp. 581-591, 1987.

Churnside, J. H., Turbulence effects on the Geodynamics Laser Ranging System, NOAA Technical Memorandum ERL WPL-218, January 1992.

Degnan, J. J., Physical processes affecting the performance of

Page29.jpg

high-power, frequency-doubled short pulse laser systems: analysis, simulation, and experiment, Ph.D. Dissertation, University of Maryland, College Park, MD, May 1979.

Degnan, J. J., Satellite Laser Ranging: Current status and future prospects, *IEEE Trans. on Geoscience and Remote Sensing*, GE-23, pp. 398-413, 1985.

Degnan, J. J., An overview of NASA SLR stations and their performance, presented at the Seventh International Workshop on Laser Ranging Instrumentation, Matera, Italy, October, 1989.

Degnan, J. J., Applications of laser ranging to ocean, ice, and land topography, *SPIE Proceedings*, Vol. 1492, Earth and Atmospheric Remote Sensing, 1991.

Degnan, J. J., and B. J. Klein, Optical antenna gain: 2. Receiving antennas, *Applied Optics*, 13, pp. 2397-2401, 1974. *Erratum: Applied Optics*, 13, p. 2397, 1974.

Degnan, J. J., B. P. Conklin, S. W. Bucey, V. S. Husson, and W. M. Decker, Baseline rates from orbit-free geometric SLR solutions, poster paper presented at Crustal Dynamics Project Investigators' Meeting, Pasadena, CA, March 4-6, 1991.

Fante, R. L., Electromagnetic beam propagation in turbulent media, *Proc. IEEE*, 63, pp. 1669-1692, 1975.

Fante, R. L., Electromagnetic beam propagation in turbulent media; an update, *Proc. IEEE*, 68, pp. 1424-1443, 1980.

Fitzmaurice, M. W., P. O. Minott, J. B. Abshire, and H. E. Rowe, Prelaunch testing of the Laser Geodynamic Satellite (LAGEOS), NASA Technical Paper 1062, October 1977.

Gaignebet, J., F. Baumont, J. L. Hatat, K. Hamal, H. Jelinkova, and I. Prochazka, Two wavelength ranging on ground target using Nd:YAG 2HG and Raman 0.68 μm pulses, Proceedings of the Sixth International Workshop on Laser Ranging Instrumentation, Antibes-Juan Les Pins, France, September 22-26, 1986.

Gardner, C. S., Effects of random path fluctuations on the accuracy of laser ranging systems, *Applied Optics*, 15, pp. 2539-2545, 1976.

Hall, F. F. Jr., M. J. Post, R. A. Richter, G. M. Lerfald, and R. E. Derr, Cirrus Cloud Model, in *Atmospheric Transmittance Radiance: Computer Code LOWTRAN* by F. X. Kneizys et al., Eds, AFGL-TR-83-0187, Air Force Geophysics Laboratory, Hanscom AFB, MA, pp. 58-67, 1983.

Hauser, J. P., Effects of deviations from hydrostatic equilibrium on atmospheric corrections to satellite and lunar laser range measurements, *J. Geophysical Research*, 94, pp. 10,182-10,186, 1989.

Herring, T. A., Marini and Murray atmospheric range correction formula, Report to the CSTG SLR Subcommission Meeting, Munich, FRG, October 18-20, 1988.

Himwich, W. E., D. S. MacMillan, C. Ma, J. W. Ryan, T. A. Clark, M. M. Watkins, R. J. Eanes, B. E. Schutz, and B. D. Tapley, The consistency of the scale of the Terrestrial Reference Frames from SLR and VLBI data, this volume, 1993.

Hufnagel, R. E., Variations of atmospheric turbulence, in *Technical Digest of Topical Meeting on Optical Propagation through Turbulence*, Optical Society of America, 1974.

International Association of Geodesy, Resolution No. 1 of the 13th General Assembly, *Bulletin Geodesique*, 70, 360, 1963.

Karp, S., R. M. Gagliardi, S. E. Moran, and L. B. Stotts, *Optical Channels: Fibers, Clouds, Water, and the Atmosphere*, Plenum Press, New York, 1988.

Klein B. J., and J. J. Degnan, Optical antenna gain. 1. Transmitting antennas, *Applied Optics*, 13, pp. 2134-2140, 1974.

Lerch, F.J., R. S. Nerem, B. H. Putney, T. L. Felsentreger, B. V. Sanchez, S. M. Klosko, G. B. Patel, R. G. Williamson, D. S. Chinn, J. C. Chan, K. E. Rachlin, N. L. Chandler, J. J. McCarthy, J. A. Marshall, S. B. Luthcke, D. W. Pavlis, J. W. Robbins, S. Kapoor, and E. C. Pavlis, Geopotential models of the Earth from satellite tracking, altimeter, and surface gravity observations, *NASA Technical Memorandum 104555*, January 1992.

Lutz, H., W. Krause, and G. Barthel, High precision two color spaceborne laser ranging system for monitoring geodynamic processes, *Space 2000*, American Institute of Aeronautics and Astronautics, New York, 1983.

Marini, J. W., and C. W. Murray, Correction of laser range tracking data for atmospheric refraction at elevations above 10 degrees, *NASA Report X-591-73-351*, Goddard Space Flight Center, 1973.

McDonnell Douglas Corporation, Synthesis and analysis of precise spaceborne laser ranging systems, Report MDC E1729, Volume I Final Report, August 1977.

Minott, P. O., Design of retrodirector arrays for laser ranging of satellites, *NASA TM-X-723-74-122*, Goddard Space Flight Center, March 1974.

Minott, P. O., Reader's Guide to the Retro Program Output, *NASA TM-X-722-76-267*, Goddard Space Flight Center, September 1976.

Ochs G. R., and R. S. Lawrence, Measurements of laser beam spread and curvature over near horizontal atmospheric paths, *ESSA Boulder Colorado Report*, ERL 106-WPL-6, February 1969.

Owens, J. C., Optical refractive index of air: Dependence on pressure, temperature, and composition, *Applied Optics*, 6, 51-58, 1967.

Pratt, W. K., *Laser Communications Systems*, pp. 121-135, John Wiley and Sons, New York, 1967.

Prochazka, I., K. Hamal, and B. Sopko, Subcentimeter single photon ranging all solid state detection package, Internal Report, Czech Technical University, July 1990.

Prochazka, I., K. Hamal, G. Kirchner, M. Schelev, and V. Postovalov, Circular streak camera application for satellite laser ranging, presented at SPIE Conference on Electronic Imaging, San Jose, California, February 24-27, 1991.

Ray, J. R., C. Ma, J. W. Ryan, T. A. Clark, R. J. Eanes, M.M. Watkins, B. E. Schutz, and B. D. Tapley, Comparison of VLBI and SLR geocentric site coordinates, *Geophysical Research Letters*, 18, pp. 231-234, 1991.

RCA Electro-Optics Handbook, Technical Series EOH-10, RCA Commercial Engineering, Harrison, NJ, 1968.

Ricklin, J. C., Optical turbulence effects on gaussian beam propagation in the unstable surface boundary layer, Master's

Page30.jpg

Thesis, New Mexico State University, Las Cruces, NM, December 1990.

Robertson, D., presented at 1991 East Coast VLBI Meeting, Lowell, Massachusetts, September 1991.

Sasaki, M., and H. Hashimoto, Launch and observation program of the Experimental Geodetic Satellite of Japan, *IEEE Trans. on Geoscience and Remote Sensing*, GE-25, pp. 526-533, September 1987.

Sasiela, R. J., A unified approach to electromagnetic wave propagation in turbulence and the evaluation of multiparameter integrals, Technical Report 807, MIT Lincoln Laboratory, Lexington, MA, 1988.

Shelus, P. J., R. L. Ricklefs, A. L. Whipple, and J. R. Wiant, Lunar laser ranging at McDonald Observatory (1969-1992), this volume, 1993.

Slater, P. N., *Remote Sensing: Optics and Optical Systems*, Chapter 13, Addison-Wesley Publishing Co., Reading, Massachusetts, 1980.

Smith, D. E., R. Kolenkiewicz, P. J. Dunn, J. W. Robbins, M. H. Torrence, S. M. Klosko, R. G. Williamson, E. C. Pavlis, N. B. Douglas, and S. K. Fricke, Tectonic motion and deformation from satellite laser ranging to LAGEOS, *J. Geophysical Research*, 93, pp. 22,013-22,041, 1990.

Varghese, T., and M. Heinick, Subcentimeter multiphotoelectron satellite laser ranging, Proc. Sixth International Workshop on Laser Ranging Instrumentation, Antibes-Juan Les Pins, France, Sept. 22-26, 1986.

Varghese, T., V. Husson, S. Wetzel, J. Degnan, and T. Zagwodzki, Intercomparison of satellite laser ranging accuracy of three NASA stations through collocation, *SPIE Proceedings*, 887, pp. 64-71, 1988.

Varghese, T., C. Steggerda, M. Selden, T. Oldham, and J. Degnan, High-resolution vidicon-based readout system for photon-counting streak camera applications, SPIE Electronic Imaging Symposium, San Jose, CA, February 1992.

Varghese, T., C. Clarke, T. Oldham, and M. Selden, Streak camera based SLR receive system for high accuracy multiwavelength atmospheric differential delay measurements, this volume, 1993.

Veillet, C., J. F. Mangin, J. E. Chabaudie, C. Dumoulin, D. Feraudy, and J. M. Torre, Lunar Laser Ranging at CERGA for the ruby period (1981-1986), this volume, 1993.

Walters, D. L., and K. E. Kunkel, Atmospheric modulation transfer function for desert and mountain locations: the atmospheric effects on r_o, JOSA, 71, pp. 397-409, 1981.

Zagwodzki, T. W., J. F. McGarry, A. Abbott, J. W. Cheek, R. S. Chabot, J. D. Fitzgerald, and D. A. Grolemund, Streak camera returns from the Relay Mirror Experiment (RME) satellite at Goddard Space Flight Center's 1.2m telescope facility, this volume, 1993.

Zwicker, H. R., Photoemissive detectors, in *Optical and Infrared Detectors*, Ed. R. J. Keyes, Springer Verlag, New York, 1977.

John J. Degnan, Code 920.1, Space Geodesy and Altimetry Projects Office, Laboratory for Terrestrial Physics, NASA/Goddard Space Flight Center, Greenbelt, MD 20771.

Page31.jpg